ABSTRACT

MAGNETIC RECONNECTION IN SMALL AND LARGE SCALES ON THE SUN

by
Xin Chen

Almost all solar activities observed are related to the solar magnetic field, especially the topological restructuring of magnetic fields, the so-called magnetic reconnection in solar physics. They are occurring at different scales related to various phenomena, during minimum or maximum of the solar cycle, from the photosphere to the solar corona.

For small-scale activities, type II spicules which display high velocity upflows observed at the limb, have the most possible underlying driving mechanism of magnetic reconnection. A set of tools is developed for detecting small-scale solar magnetic cancellations and the disk counterpart of type II spicules (the so-called Rapid Blueshifted Excursions, RBEs), using line-of-sight photospheric magnetograms and chromospheric spectroscopic observations, respectively. These tools are further employed to analyze coordinated observation using the Interferometric BIdimensional Spectrometer at the Dunn Solar Telescope of the National Solar Observatory and *Hinode*. The statistical properties of magnetic cancellations and RBEs are presented and their correlation is explored using this data set.

For large-scale activities, recent high resolution extreme-ultraviolet observation from the Solar Dynamics Observatory (SDO) is able to diagnose the plasma around current sheet, the key role of magnetic reconnection during energetic solar flares. Supra-arcade downflows (SADs) have been frequently observed during the gradual phase of flares near the limb. In coronal emission lines sensitive to flaring plasma, they appear as tadpole-like dark voids against the diffuse fan-shaped "haze" above the well-defined flare arcade and flow toward the arcade. Several selected SADs from two flare events are carefully studied. Their differential emission measures (DEMs) and DEM-weighted temperatures are calculated using data obtained by the Atmospheric Imaging Assembly onboard SDO. This analysis corroborates that SADs are density depletion associated with a substantial decrease in DEM. This depression in DEM rapidly recovers in the wake of the SADs studied, generally within a few minutes, suggesting that they are discrete features. In addition, SADs in one event are found to be spatio-temporally associated with the successive formation of post-flare loops along the flare arcade.

MAGNETIC RECONNECTION IN SMALL AND LARGE SCALES ON THE SUN

by
Xin Chen

A Dissertation
Submitted to the Faculty of
New Jersey Institute of Technology and
Rutgers, The State University of New Jersey – Newark
in Partial Fulfillment of the Requirements for the Degree of
Doctor of Philosophy in Applied Physics

Department of Physics

May 2016

APPROVAL PAGE

MAGNETIC RECONNECTION IN SMALL AND LARGE SCALES ON THE SUN

Xin Chen

Dr. Haimin Wang, Dissertation Co-Advisor Date
Distinguished Professor of Physics, Director of Space Weather Research Laboratory,
Chief Scientist of Big Bear Solar Observatory, NJIT

Dr. Na Deng, Dissertation Co-Advisor Date
Research Professor of Physics, NJIT

Dr. Camelia Prodan, Committee Member Date
Associate Professor of Physics, NJIT

Dr. Cristiano Luis Dias, Committee Member Date
Assistant Professor of Physics, NJIT

Dr. Martin Schaden, Committee Member Date
Associate Professor, Director of Graduate Program in Applied Physics,
Rutgers University, Newark

Dr. Rui Liu, Committee Member Date
Professor of Geophysics and Planetary Sciences, University of Science and
Technology of China, Hefei, Anhui, China

BIOGRAPHICAL SKETCH

Author: Xin Chen

Degree: Doctor of Philosophy

Date: May 2016

Undergraduate and Graduate Education:

- Doctor of Philosophy in Applied Physics,
  New Jersey Institute of Technology, Newark, NJ, 2016
- Bachelor of Science in Astronomy,
  Nanjing University, Nanjing, Jiangsu, China, 2009

Major: Applied Physics

Publications:

Chen, Xin; Liu, Rui; Deng, Na; Wang, Haimin, "Thermodynamics of Supra-Arcade Downflows in Solar Flares," 2016, ready to submit

Chen, Xin; Deng, Na; Lamb, Derek A.; Jing, Ju; Liu, Chang; Liu, Rui; Park, Sung-Hong; Wang, Haimin, "Development of Technique to Detect and Classify Small-Scale Magnetic Flux Cancellation and Rapid Blue-Shifted Excursions," 2015, *Research in Astronomy and Astrophysics*, 15, 1012

Deng, Na; Chen, Xin; Liu, Chang; Jing, Ju; Tritschler, Alexandra; Reardon, Kevin P.; Lamb, Derek A.; Deforest Craig E.; Denker, Carsten; Wang, Shuo; Liu, Rui; Wang, Haimin, "Chromospheric Rapid Blueshifted Excursions Observed with IBIS and Their Association with Photospheric Magnetic Field Evolution," 2015, *The Astrophysical Journal*, 799, 219

Deng, Na; Tritschler, Alexandra; Jing, Ju; Chen, Xin; Liu, Chang; Reardon, Kevin P.; Denker, Carsten; Xu, Yan; Wang, Haimin, "High-Cadence and High-Resolution Hα Imaging Spectroscopy of a Circular Flare's Remote Ribbon with IBIS," 2013, *The Astrophysical Journal*, 769, 112

Presentations:

Chen, X.; Liu, R.; Deng, N.; Wang, H., "Dynamical Thermal Structure of Super-arcade Downflows in Solar Flares," *Dissertation Talk*, Joint American Astronomical Society/American Geophysical Union Triennial Earth-Sun Summit meeting 1, Minneapolis, IN, 2015.

Chen, X.; Deng, N.; Lamb, D.; Jing, J.; Tritschler, A.; Reardon, K. P.; Wang, H., "Statistical Study of Magnetic Cancellations and On-disk Type-II Spicules," American Astronomical Society Solar Physics Division meeting 44, Bozeman, MT, 2013.

Deng, N.; Tritschler, A.; Jing, J.; Chen, X.; Liu, C.; Reardon, K. P.; Denker, C.; Xu, Y.; Wang, H., "High-Cadence and High-Resolution Hα Imaging Spectroscopy of a Circular Flare's Remote Ribbon with IBIS," American Astronomical Society Solar Physics Division meeting 44, Bozeman, MT, 2013.

Deng, N.; Tritschler, A.; Jing, J.; Chen, X.; Reardon, K.; Liu, C.; Xu, Y.; Wang, H., "Hα Imaging Spectroscopy of a C-class Flare with IBIS," Science with Large Solar Telescopes, Proceedings of IAU Special Session 6, Beijing, china, 2012.

Chen, X., Deng, N.; Jing, J.; Tritschler, A.; Reardon, K.; Wang, H., "Coordinated Observations of On-disk Type II Spicules with IBIS and Hinode," American Astronomical Society meeting 220, Anchorage, Alaska, 2012.

Deng, N.; Tritschler, A.; Jing, J.; Chen, X.; Reardon, K.; Liu, C.; Xu, Y.; Wang, H., "High Cadence and High Resolution Hα Imaging Spectroscopy of a C4.1 Flare with IBIS," American Astronomical Society meeting 220, Anchorage, Alaska, 2012.

To my parents: Duan Chen and Chong Zheng

献给我的父亲母亲：陈端 和 郑冲

ACKNOWLEDGMENT

First and foremost, I would like to express my special appreciation and thanks to my co-advisor Dr. Haimin Wang for his great mentoring and brilliant research ideas. He provided me much valuable guidance and inspiration throughout the Ph.D. study, not only in my academic education but also in personal life. He offered me the opportunity and generous financial support to further step into the world of solar physics, enlightened me with his great wisdom and kindness. It is surely an honor for me to be his Ph.D. student.

My sincere gratitude also goes to my co-advisor Dr. Na Deng, for her considerate advice and encouragement. She spent so much time and energy on my papers and data analyses. She was always amiable during discussions and easy to access. I heartily appreciate her support and help.

I deeply thank all of my committee members: Dr. Rui Liu, Dr. Cristiano Luis Dias, Dr. Camelia Prodan and Dr. Martin Schaden for taking the time to revise this dissertation and to be my thesis committee members. It is with immense gratitude that I acknowledge the support and help of Dr. Rui Liu. He provided much insightful direction and feedback. This thesis would not have been possible without his tremendous time and effort.

In particular, I sincerely appreciate Dr. Alexandra Tritschler from National Solar Observatory for her sustained help of data processing, as well as Dr. Derek A. Lamb and Dr. Craig E. DeForest from Southwest Research Institute for their patient instruction of SWAMIS algorithm.

This research was supported by NASA under grants NNX11AO70G, NNX13AF76G and NNX14AC12G and by NSF under grants AGS 1153226, 1250374, 1348513 and 1408703.

I am also grateful to acknowledge the following organizations for their financial supports: the Solar Physics Division of the American Astronomical Society for traveling funds to attend the 2012 annual conference and the SDO 2013 Science Workshop; the National Science Foundation and the Center for Space Plasma and Aeronomic Research at the University of Alabama in Huntsville for the stipend supporting my travel to the 2013 Space Weather Summer School.

It is my fortunate to appreciate the researchers in our NJIT solar group: Drs. Chang Liu, Ju Jing, Yan Xu, Wenda Cao, Gregory Fleishman, Gelu Nita, Bin Chen, Jeongwoo Lee, Shuo Wang, Yixuan Li, Yuan Yuan, Kyung-guk Min and Samuel Tun. I enjoyed researching with them and learned a lot from them in these years. Thanks to my schoolmates: Zhicheng Zeng, Zhitao Wang, Xiupeng Wang, Shaheda Begum Shaik, Natsuha Kuroda, Xu Yang, Qin Li, Nengyi Huang, Jiasheng Wang and also to all my friends and colleagues at NJIT.

I wish to thank all the rest of the academic and support staff of the Center for Solar-Terrestrial Research and New Jersey Institute of Technology for providing resources and support. Special thanks go to Ms. Christine Oertel and Ms. Cheryl James, the administrative assistants in our center, for assisting me in many ways.

Lastly, but importantly, I want to express my heartfelt thanks to my parents, Duan Chen and Chong Zheng. Without their consistent love and support, I can not complete my dissertation.

TABLE OF CONTENTS

Chapter **Page**

TABLE OF CONTENTS
(Continued)

Chapter **Page**

LIST OF TABLES

Table **Page**

LIST OF FIGURES

LIST OF FIGURES
(Continued)

LIST OF FIGURES
(Continued)

LIST OF FIGURES
(Continued)

LIST OF FIGURES
(Continued)

CHAPTER 1

INTRODUCTION

1.1 The Sun

The Sun is undoubtedly the most important star for our humankind on the Earth, emphasized by name of NASA's new program "Living with a star". As the nearest star, the distance from the Sun to the Earth is about 1.496×10^8 km, which is significantly less ($\sim 10^{-5}$) than the second closest star, Alpha Centauri. Thus, till now the Sun is the only star that can be observed and studied in detail.

Generally, the Sun can be stratified into several spherical shells of different physical characteristics. At the center region within 0.25 solar radius ($R_\odot = 6.963 \times 10^5$ km; Emilio et al. 2012) is the core of the Sun, where the nuclear fusion occurs. The proton-proton chain reaction generates most of energy that are transported out of the core. From the 0.25 $R_\odot$ to about 0.75 $R_\odot$ is the radiative zone since the energy produced from the core are propagated by radiation in this region. From 0.75 $R_\odot$ to the surface of visible light (1 $R_\odot$) is the convective zone, where the thermal convective motion dominates the flows of material and energy. The surface (and $R_\odot$) is defined by a very thin layer ($\sim$ 100 km) named photosphere since it is where emits most of visible light to be seen from the Earth. Start from the photosphere, regions $\geq 1R_\odot$ is the solar atmosphere, including chromosphere and corona, which will be introduced in Section 1.2.

The interior structure of the Sun is mainly studied by modeling using observational characteristics since it is below the photosphere where can not be directly observed. Numerous observations have revealed that the Sun has differential rotation, i.e., the angular velocity of longitudinal rotating on the surface is dependent on the latitude. Besides, the meridional flows have also been confirmed that is the latitudinal flows. Furthermore, analyses of photospheric velocity fields discover the 5 minute oscillation (Leighton et al. 1962), which is vertical motions respect to the surface. All these phenomena are connected in the interior structure of the Sun. The differential rotation only exhibits above the tachocline layer (the thin layer separating the radiative zone and convective zone), however, the inner regions rotate uniformly. Meridional flows are connected in the convective zone as circulations. In addition, the study of wave propagation inside the Sun similar to the earthquake wave is also developed and named helioseismology, which becomes a powerful tool to explore the structure of the interior as well as the backside of the Sun.

After centuries of observations, it has been well known that the Sun has a periodic variation of activity for about every 11 years, called the solar cycle (Figure 1.1). This cyclic behavior is mainly represented by the number of sunspots (the dark spot in the photosphere), corresponding solar activities and solar irradiance. Moreover, the global magnetic dipole structure of the Sun gradually switches to the opposite polarity in every cycle. The study of solar cycle found that the Sun also has non-periodic variation between cycles, e.g., the period would be slight deviated from 11 years, as well as scale or duration of each solar maximum can vary to a certain context.

Magnetism is ubiquitous on the Sun and always plays an important role in solar activities. The magnetic fields can be extremely strong, reach $\sim$ 3500 G in active

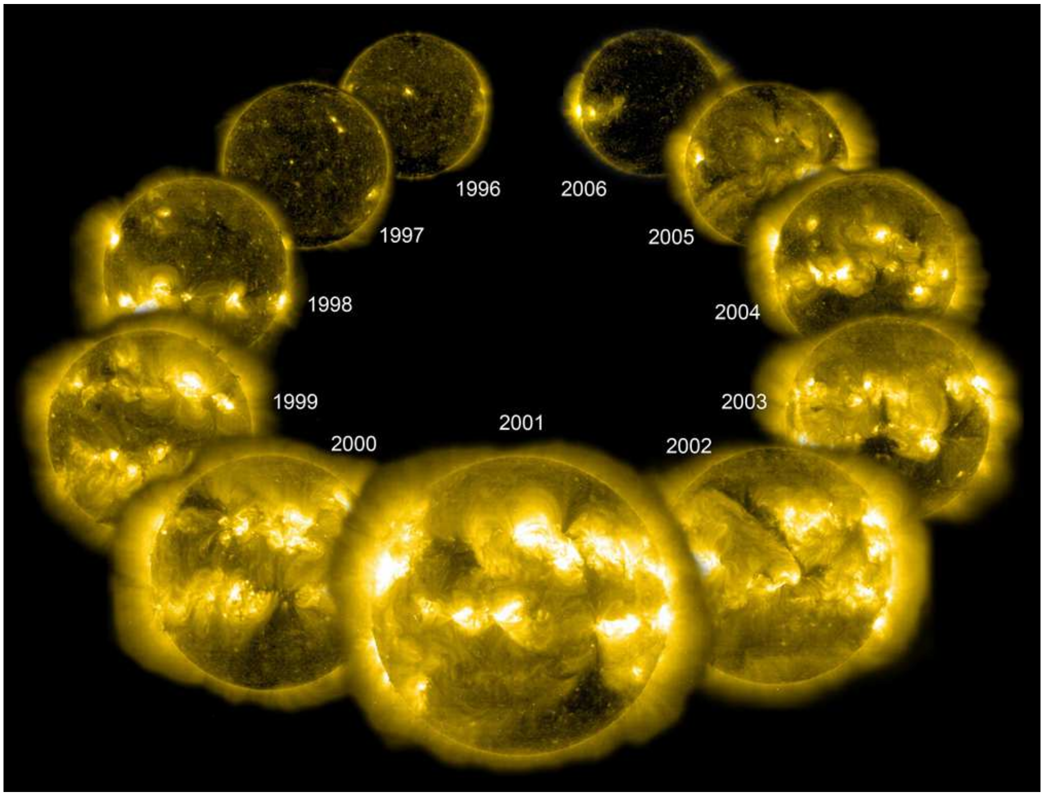

Figure 1.1 Illustration of a completed solar cycle observed by Solar and Heliospheric Observatory (SOHO) in extreme-ultraviolet wavelength (171 Å), which shows the relative activity of the Sun (Courtesy of NASA).

regions concentrated at the sunspots. Even in the quiet sun regions, they are not tranquil but showing network and intra-network structures. Solar activities in all levels are related to the change of magnetic field configuration, especially in a form named magnetic reconnection which is introduced in Section 1.3.

As a star, the Sun also loses its mass mainly through a quasi-steady particle flow, the solar wind. Propelled by the energy provided from the interior and propagated through the solar atmosphere, some particles in the corona could obtain enough energy to escape the gravity of the Sun. The solar wind and its associated magnetic field spread across the solar system with bubble-like shape which is called heliosphere.

Certainly the Earth is influenced by these solar energetic particles, produces as related geomagnetic effects (e.g., aurora). The solar wind also exhibits variations caused by the activities in the solar atmosphere, which is the critical information to explore how it is formed and what would consequently affect the Earth.

Flares and coronal mass ejections (CMEs) are the most energetic activities in the solar atmosphere. Flares were initially observed as a suddenly brightening in the Hα spectrum (a chromospheric emission line), and after decades of study people find the diversity of flares and their complicated observational characteristics in all wavelengths, from radio to hard X-ray (HXR). In principle, flare is a dynamic process that releases the magnetic free energy, due to the change of the magnetic topology though magnetic reconnection, resulting in heating of the plasma and acceleration of particles. More details and flare models will be introduced in Section 1.4.1. Closely related to flares, CMEs are also extremely eruptive processes of the largest spatial scale in the solar system. Generally, $10^{11} \sim 10^{13}$ kg materials, packaged with magnetic flux, are rapidly ($100 \sim 2000$ km s^{-1}) ejected away from the corona, presented as transient brightening moving away from the sun using coronagraph observation. After CME eruption, this ejected magnetized plasma continuous propagates in the interplanetary space, called interplanetary CME. Some of them would approach the Earth, which could affect the magnetosphere and the ionosphere of the Earth.

As the development of science and exploring of space, it becomes important to realize the effect and potential endangerment coming from the Sun to the near-earth space, which promote an interdisciplinary science called space weather. The highly energetic particles from the solar wind, irradiance of flares, and interplanetary

CMEs sometimes could cause intensive disturbance in the higher atmosphere of the Earth, most notably the magnetic storms. This disturbance, especially originated from solar eruptive activity, has potential to bring disastrous environment near the earth, threatening the satellites, astronauts, even daily activities such as aviation and Global Position System (GPS). Thus, the study of the Sun which studies the source of space weather becomes increasing important in nowadays. It is not only revealing the mechanism of activities on the closest star, but also providing the theoretical basis for the forecast of devastating space weather effects.

1.2 Solar Atmosphere

The solar photosphere has the longest observational history since it is the surface of the Sun in visible light. As mentioned above, the radius of the photosphere is 1 $R_\odot$, i.e., 6.963×10^5 km. Most of solar radiation is emitted from the photosphere that is similar to a black body, as the effective temperature of the photosphere can be found as $\sim$ 5800 K using Stefan-Boltzmann Law. Its density is derived through modeling, generally $\sim$ 0.2 g m^{-3}.

Although the majority area of photosphere appears to be uniform, it exhibits as granule-like pattern with high spatial resolution observations (Figure 1.2). This granulation reflects convective clusters from interior that arrive to the photosphere. Each granule shows a bright center with upward motion and grows in size (from $< 1''$ to $3'' \sim 5''$), until finally fragments after several minutes. Using the Doppler map, supergranulation (Leighton et al. 1962) has been found which is a much larger convective velocity field structure than granules, with a size of $\sim 30''$. The

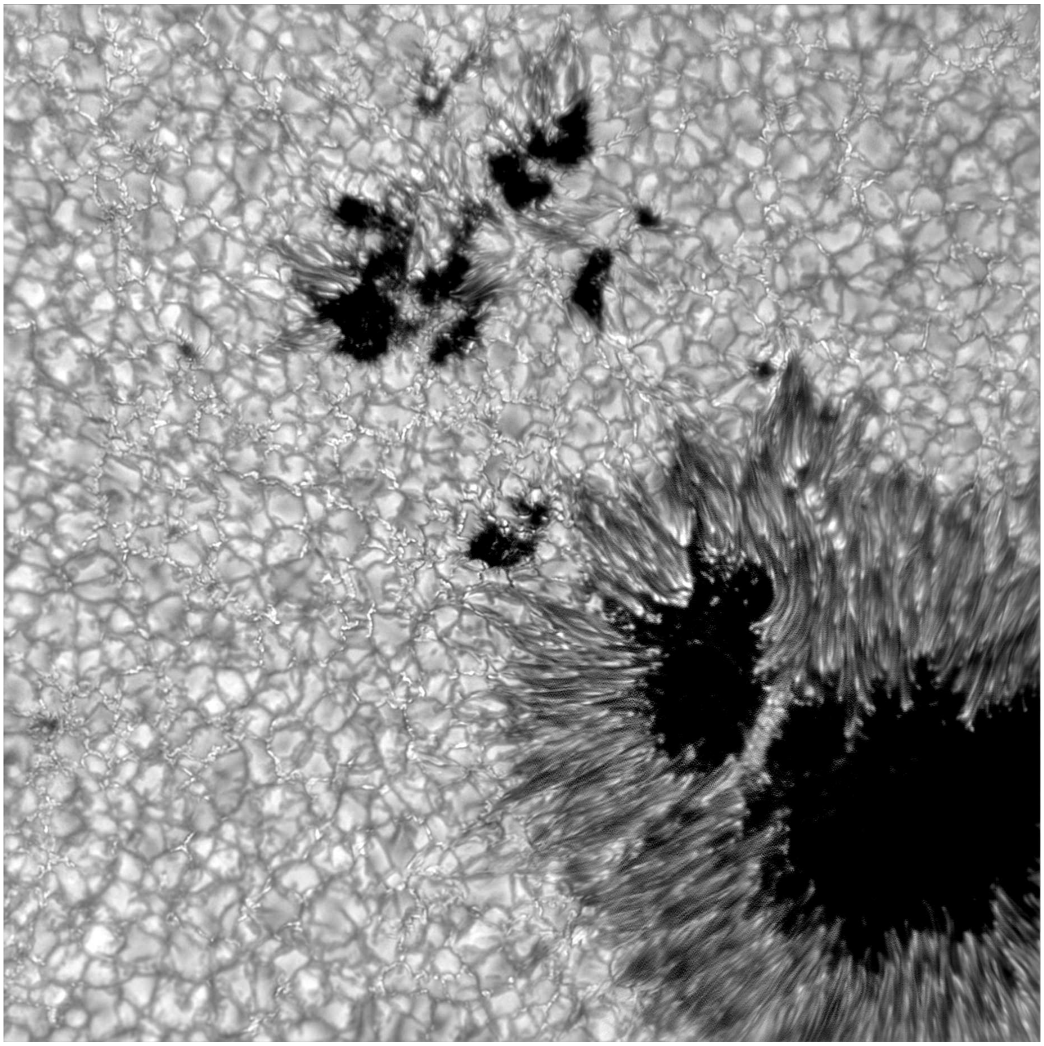

Figure 1.2 High resolution image of sunspot (lower right) and granules (except lower right and upper middle) observed by New Solar Telescope (NST) at Big Bear Solar Observatory (BBSO; Courtesy of BBSO and Ciel et Espace).

supergranulation is almost indistinguishable on the white-light image (continuum intensity). However, the boundary of supergranules does coincide with the magnetic network field and connect to the chromosphere rosette structure.

The sunspots are prominent structure in the photosphere as dark islands in the sea of light (Figure 1.2). The darkest core of the sunspot is called umbral and the surrounded less darker region is penumbral. The weak emission indicates their lower temperature, generally $\sim$ 4800 K at the umbral. Sunspots typically emerges in pairs (of opposite magnetic polarities). They may appear in clusters during the solar maximum, within the region of 40 degrees around the equator. Their emergence shows a pattern in each solar cycle, starts from high latitude of both hemispheres then gradually migrates to lower latitude. Generally, the sunspots exist from several days to more than one month. During this time, they keep evolving with some of the larger ones can expand to dozens or even hundreds of arcseconds. The velocity field shows there is a persistent flow across the penumbral, from the umbral side to the outside of the sunspot called Evershed flow (Evershed 1909). The sunspots also exhibit a significantly stronger magnetic field than any other places in the photosphere. Most eruptive solar activities occur in active regions consisting of sunspots, especially in those larger ones including several sunspots entangled with each other.

The chromosphere is the atmospheric shell above the photosphere. It has much less emission than the photosphere due to its low density ($\sim 10^{-4}$ g m^{-3}). It was only observable at the solar limb during the total solar eclipse. Until the availability of spectroscopy in the last century, the whole chromosphere is revealed in its emission line (e.g., Hα and Ca II, see Figure 1.3). Unlike the inner shells, the temperature is increasing with height in the chromosphere. Generally, the temperature minimum ($\sim$ 4000 K) between the photosphere and the chromosphere is considered as the boundary between them. The upper boundary separating the chromosphere and corona is a thin layer named transition region where the temperature rapidly increases from 10^4 K to 10^6 K. The relatively uniform chromosphere has a thickness of 1500 km.

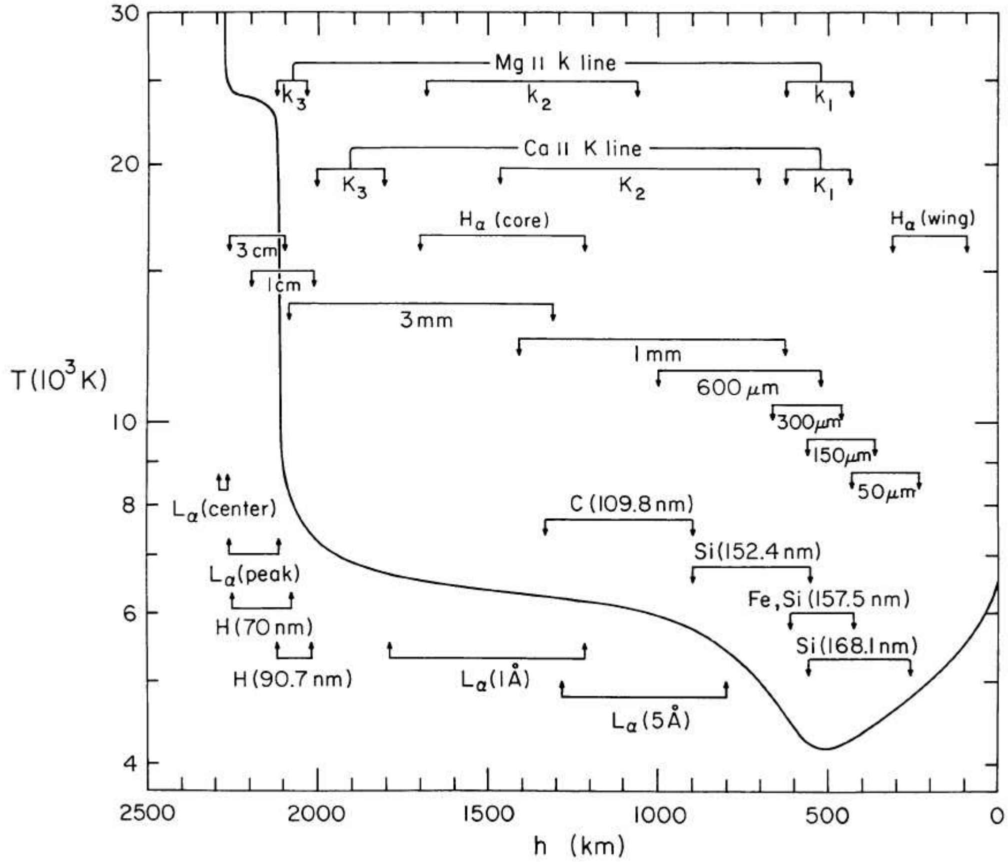

Figure 1.3 General temperature distribution by height (above solar surface) and formational regions of various spectral observations including Hα and Ca II (Vernazza et al. 1981).

However, it contains pine-like structures called spicules which could reach $\sim$ 5000 km through limb observation.

The quiet sun and active region (AR) also exhibit different structure in the chromosphere. When observing the disk using chromospheric lines, there are relatively brighter regions called plages which correspond to AR and the sunspots in the photosphere. From high resolution Hα spectroscopic observation, bright and dark fibrils can be seen inside or around plages, which show the traces of plasma as well as magnetic fields. Besides plages, the quiet region of chromosphere presents a rosette structure that can be either bright or dark based on the specific spectrum characteristics. As mentioned above, the chromosphere rosette pattern shows a close relation with supergranule boundaries and magnetic network fields in the photosphere in sizes and locations.

The corona is the outermost layer of solar atmosphere. It is more rarefied ($n_e \simeq 10^{-9} \sim 10^{-6}$ cm^{-3}) and extended than the chromosphere and of extremely high temperature ($> 10^6$ K). One way to observe the corona is using coronagraph, an instrument that blocks the photosphere and chromosphere in order to resolve the corona. It can also be observed using radio observation and space telescope that avoids the absorption from the Earth's atmosphere in the extreme-ultraviolet (EUV) and X-ray wavelengths. The corona presents that it is non-uniform, i.e., has structures in many scales.

In the corona, the active regions and quiet sun can be obviously distinguished by the contrast, as well as the coronal holes, the darkest regions. The coronal holes are extremely rarefied since they are regions of open magnetic fields where the plasma is efficiently transported from the corona into the solar wind. Except the coronal holes, there are several non-uniform structures in the corona, such as streamers, loop arcades and filaments (prominences) etc. The streamers are radially outward elongation can reach more than 1 $R_\odot$. The loop arcades show the 3D configuration of magnetic fields and corresponding plasma, mostly inside or between active regions.

The filaments are the dark cloud-like structure on the disk observations, which is exactly the same as prominences, the bright raised structure at the limb. Their emission is weaker than the photosphere but greater than the chromosphere background, thus, shows different appearance. The filaments are extended from the chromosphere to the corona and have various shapes. They are cooler and denser plasma, which can exist for a long period (a few to more than a hundred days). However, in specific scenarios, they are also able to erupt quickly (in minutes).

The corona has a significantly higher temperature than the chromosphere and the photosphere, thus, how the corona maintains its temperature is a persistent puzzle in solar physics, the coronal heating problem (Hollweg & Buti 1985). Based on the second law of thermodynamics, the temperature of the solar atmosphere should gradually decrease with radial distance, unless there is a mechanism to continuously heat the corona. It has been found that although the eruptive solar activities like flares and CMEs release numerous energy from the photosphere, their occurrence rate is too low which only contributes a small part to the coronal heating. Activities with smaller scale, such as microflares (van Speybroeck et al. 1970), nanoflares (Parker 1988) and jets actually contribute much more to the energy balance than the larger scale activities. There are many models of coronal heating and generally can be classified into two types (Klimchuk 2006). One is DC (Direct Current) models, focus on magnetic reconnection, current cascades etc. The other one is AC (Alternating Current) models, focus on alfvenic resonance, resonant absorption etc. These models remain to be examined by the observational evidence.

1.3 Magnetism

Magnetic fields are omnipresent in every aspect of solar physics. The solar magnetic fields have a complicated distribution and keep evolving. Observationally, only photospheric magnetic fields can be relatively accurately measured using Zeeman effects. For the chromosphere, this measurement of magnetic field is less accurate. For the corona, it is only accessible at the strong fields, e.g., active regions, to be conjectured by gyrosynchrotron emission using radio observation. Due to the importance of magnetic fields and the difficulty of corresponding observation at solar upper atmosphere, a widely used method is extrapolation, which using photospheric magnetic fields as boundary conditions and model assumption (e.g., force-free field) to construct the most possible 3D configuration of magnetic fields.

Generally, the solar magnetic fields can be categorized into three types, active region fields, quiet sun fields and polar fields. The active regions have the strongest magnetic field on the Sun, as much as $1500 \sim 3500$ G at the umbral of sunspots (Penn & Livingston 2006). It has dipolar or more complicated multipolar structure, mostly based on the numbers of sunspots in the AR. Besides the active region fields, the quiet sun regions also have weak magnetic fields, showing the network structure named as magnetic network fields. As mentioned above, magnetic network fields correspond to the supergranule boundary and the chromospheric rosette structure. Generally, the magnitude of magnetic network fields is $20 \sim 200$ G. Through high resolution observations, it has been found that there are small-scale transient (a few to dozens of minutes) magnetic islands inside the magnetic network fields, called magnetic intra-network fields (Livingston & Harvey 1975; Harvey 1977). The quiet sun fields are mostly random without polarity bias, except at the coronal holes. The polar fields are similar to the Earth's magnetic fields with opposite polarities at each pole. However, the polar fields on the Sun would switch its polarity every solar cycle.

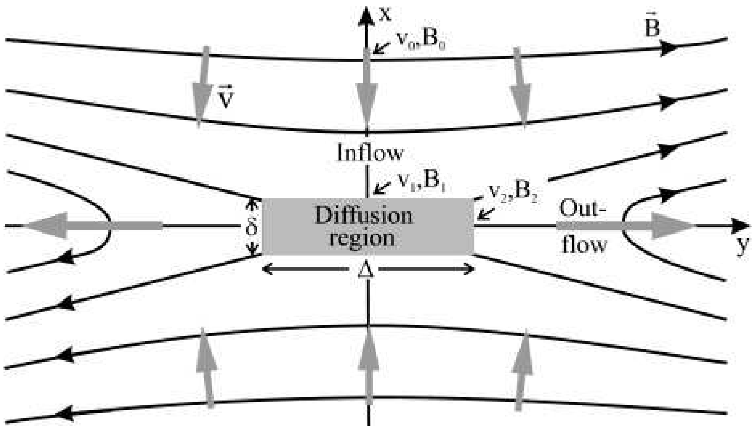

Figure 1.4 Schematic of 2D magnetic reconnection. Driven by the vertical inflows, magnetic fields of opposite direction meet at the center, reconnected with each other and then release with horizontal outflows. The center zone has relatively small R_m is the diffusion region. (Schindler & Hornig 2000)

The ubiquitous magnetic fields link to various solar phenomena through a specific process named magnetic reconnection in magneto-hydrodynamics (MHD). Especially the famous induction equation:

$$\frac{\partial \vec{B}}{\partial t} = \nabla \times (\vec{v} \times \vec{B}) + \eta \nabla^2 \vec{B}, \tag{1.1}$$

(with a constant magnetic diffusivity η)

shows that the evolution of magnetic fields depends on the convective term (the first term on the right-hand side) and the diffusive term (the second term on the right-hand side). Their ratio is called magnetic Reynolds number:

$$R_m = \frac{l_0 v_0}{\eta}, \tag{1.2}$$

(l_0, v_0 are length scale and velocity scale, respectively)

Generally in the solar atmosphere, R_m is very large ($R_m \gg 1$), which means that the convective term dominates the diffusive term. In other words, the magnetic fields are "frozen" in the plasma materials and follow their motions. However, during various solar active events, the magnetic energy is suggested to be converted into kinematic motion and heating of plasma, as well as energy for accelerating particles. This scenario requires the diffusive term to be comparable with the convective term ($R_m \sim 1$) within a much smaller length scale called diffusion region (Figure 1.4). In other words, only if the diffusion region is very thin, where an extremely strong current sheet exists, the magnetic energy can be released to drive those active events. The magnetic fields around the diffusion region must be changed in direction and magnitude as they disconnected in the diffusion region and reconnected after leaving. This topological restructuring, is called magnetic reconnection. It can occur on various active events with different scales.

1.4 Solar Activity

1.4.1 Large Scale Activities in Active Regions

As one kind of the most intense solar eruptive activities (thermal energy: $10^{30} \sim 10^{33}$ erg), flares have various shapes with significantly different characteristics. Thus, it is helpful to classify the flares, customarily into five levels, namely A, B, C, M and X. This classification is based on the soft X-ray (SXR) emission of the flare (at $1 \sim 8$ Å) observed near the earth, correspondingly between 10^{-8}, 10^{-7}, 10^{-6}, 10^{-5}, 10^{-4}, and more than 10^{-4} J m^{-2} s^{-1}. Besides this level that generally reflects the intensity of the flares, their structure and mechanism can be generalized into two types. One type is the simple-loop flares that have smaller size and generally show several brightening cores in Hα observations. The other type is the double-ribbon flares named by the obvious separating double ribbon pattern in Hα observations. This type of flares are closely related to the filament eruption and have a characteristic structure. In the corona, bright loops are sequentially appeared of increasing height, resulting in the footpoints of the loops form the double ribbon in the chromosphere. Compare to the single-loop flares, the double-ribbon flares are larger in size and represent most of high level flares.

CMEs are the representative products associated with alteration of large-scale structure of the corona and significant affect the interplanetary space. They are observable in visible (coronagraph), EUV, X-ray and radio. The typical CMEs exhibit a well-accepted three-part structure, a bright front, a dark cavity and a bright core (erupted helical filament) from the outside in (Illing & Hundhausen 1985). CMEs have very spread distribution of their observational characteristics such as size, angular width and velocity. One kind of CMEs has a much smaller angular width are called narrow CMEs, which may have a different structure and mechanism comparing to normal CMEs (Fang et al. 2008). Oppositely, halo CMEs represent those ones with huge angular width, which are normal CMEs propagating along the Sun-Earth direction. The relation between CMEs and flares keep under active investigations, however, it has been found that they are not one-to-one corresponded. There are observations showing flares with a failed eruption and filaments erupt without a flare. A further interpretation has been gradually accepted is that flares and CMEs are different perspectives of the same coherent process.

The studies of numerous flares have generalized a standard model that illustrates observational characteristics through 2D magnetic reconnections. It is named CSHKP

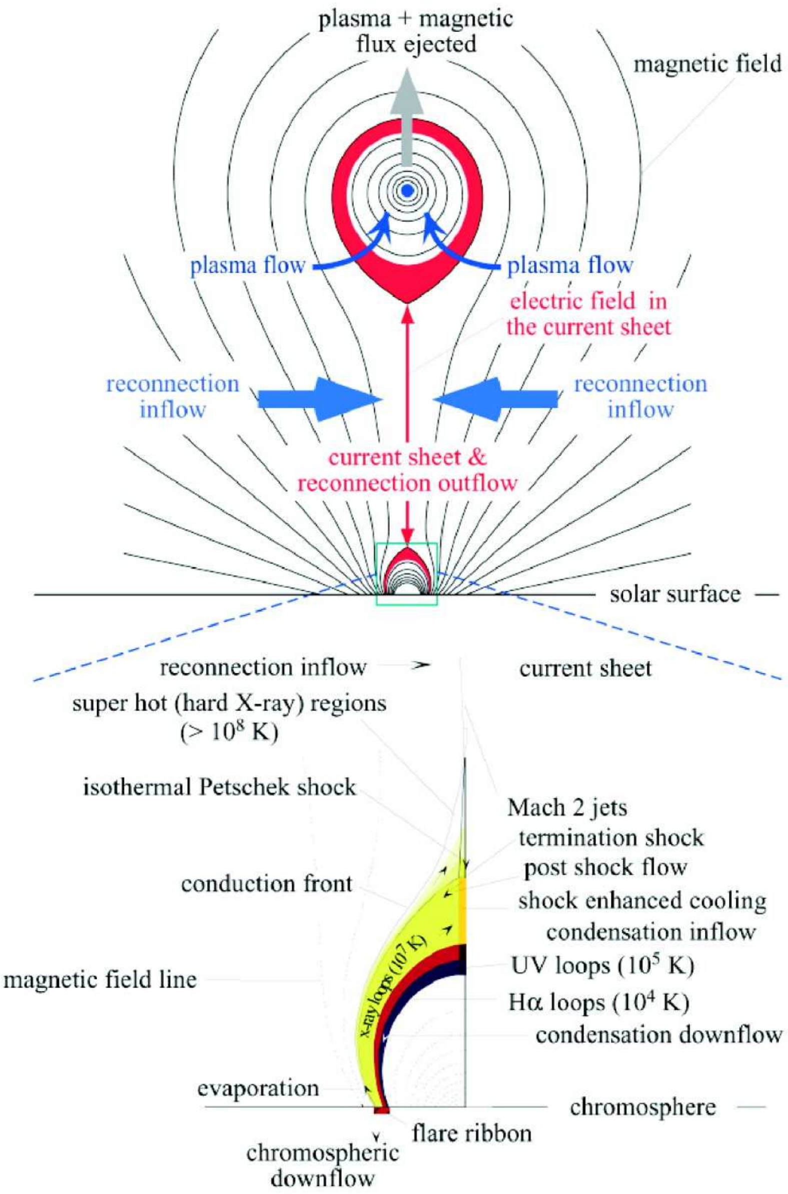

Figure 1.5 Schematic of an evolutionary model by Lin et al. (2005) in the CSHKP genre. This diagram unites the two-ribbon flare configuration of Forbes & Acton (1996) and the CME configuration of Forbes & Lin (2000). Colors in the lower panel roughly denote loops of different temperatures.

model (assembly of initials of its five authors, Carmichael 1964; Sturrock 1966; Hirayama 1974; Kopp & Pneuman 1976) that describes a raising filament stretches the magnetic fields around it into an X-type structure and then reconnection occurred.

The magnetic energy is released and the outflows of magnetic reconnection ejected in two opposite directions. On one hand, the lower one (toward to the photosphere) hit the plasma in the corona produce the loop-top HXR source and form the shockwave. The released energy is converted in the form of particles acceleration and heat conduction, which keeps flowing down to the chromosphere and deflects following the magnetic fields. In the chromosphere, the denser plasma is heated and expand bi-directional along the magnetic fields, which forms not only the post-flare loops in the corona (observable in X-ray, ultraviolet to Hα) called chromospheric evaporation, but also the Hα double ribbons. On the other hand, the upper reconnection outflows and raising filament are promising to develop into a CME, if the energy released by the flare is enough to overcome the constraint of magnetic fields. This standard model fits major observations after the raising filament and accounts the physical processes of them. (see Figure 1.5)

However, the driving mechanism of the standard model, i.e., what initially triggers the magnetic reconnections is still an open issue, thus, there are many evolutionary models. Several models present that instead of a raising filament, the evolution of photospheric magnetic fields is the essential driver of flares. For instance, the 2D model of Forbes & Priest (1995) shows that the photospheric converging flows (the flux flow towards the magnetic neutral line) can impel a stable magnetic field configuration into an eruptive flare (Figure 1.5). Their further analytically simulation present that a minor reconnection rate is able to lead a successful eruption with adequate energy released (Lin & Forbes 2000). Moreover, this simulation also predicts the evolution of current sheet as rapidly extending in length and the shrinkage of post-flare loops, which are consistent with further observations.

In addition, several other evolutionary models develop into 3D magnetic configurations, such as the magnetic breakout model (Antiochos et al. 1999), the tether-cutting model (Moore et al. 2001) etc. Different from 2D models which suppose the 2D configurations are echoed in the third dimension (generally along the magnetic neutral line), 3D models concern the evolution in the third dimension like photospheric shear flows (semi-parallel to the magnetic neutral line). The magnetic breakout model starts with a filament which constrained by a quadrupolar magnetic configuration. The photospheric shear motion stretches the magnetic fields above the filament into X-shapes and triggers the reconnection in high corona, which further removes the constraint and releases the filament as an eruption. However, the tether-cutting model states a different mechanism. In this model, the quadrupolar system is involved below the filament where the footpoints are dragged by the photospheric shear motion and from an X-shape configuration. The reconnections first occur at below and propel the raising of filament, leading further reconnections in the standard model. Both models have several specific characteristics been observed and wait for further investigation, since flares in reality are extremely complicated.

1.4.2 Small Scale Activities in the Quiet Sun

Besides the large scale activities above, numerous small scale activities have been discovered by taking the advantage of developing observational instruments. Even in the quiet Sun or coronal hole, there are SXR bright points and EUV transient brightenings in the corona. They are likely resulting from the microflares and nanoflares, respectively, which may have similar processes of flares but downgraded in scale. As a customary classification, microflares have thermal energy of $10^{27} \sim 10^{30}$ erg with SXR and EUV emission, as well as nanoflares are even smaller of $10^{24} \sim 10^{27}$ erg energy and only show EUV emission (Aschwanden 2006). Lower in the chromosphere, spicules (Beckers 1968; Suematsu et al. 1995), jets and explosive events (Brueckner & Bartoe 1983; Dere et al. 1989) in the transition region are ubiquitous tiny dynamics. All these small scale activities are more or less related to the photospheric magnetic fields evolution, even at a much weaker magnitude. Although the effects of each small scale activities are trivial comparing to flares or CMEs, their high frequency cause them to play an even more important role in the balance of energy and mass of the solar atmosphere.

Through high resolution observation of chromosphere, myriad spicules exhibit like forest with various inclinations at the limb. They are dynamics of several minutes lifetime, a few arcsecs in width and dozens arcsecs in length. The velocities of spicules are measured lower than the escape velocity of the Sun, thus, essentially they are ballistic flows that finally fall back to the photosphere. The study of spicules has been difficult since their tiny size is close to the observational resolution limit until recent years. (Sterling 2000)

Meantime, several chromospheric dynamics like jets are initially studied through the velocity field on the disk using spectroscopic analysis of chromosphere lines. By scanning the line profiles, the upward and downward flows can be diagnosed in the line wings based on the Doppler effect. Thus, dynamic processes are reflected by enhanced features that appears in the line wings without affecting the line center. A kind of phenomena only appearing in blue wing has been noticed, due to its upward motion, obtained evolutionary names such as Hα jets (Wang et al. 1998), chromospheric upflow events (Chae et al. 1998; Lee et al. 2000) and most recently, rapidly blueshifted excursions (RBEs; Langangen et al. 2008; Rouppe van der Voort et al. 2009). For explosive events, they are likely more intense that can even present emission (brightening, e.g., Ellerman Bomb; Ellerman 1917) at both blue and red winds corresponding to their bi-directional flows. These activities have sizes of similar magnitude with spicules but higher velocities and enhanced temperature.

Solar activities in the photosphere are mostly presented by magnetic field, such as magnetic flux emergence and oppositely, magnetic flux cancellation. These two magnetic events are omnipresent due to the unceasing convention flows which bring the flux up and down through the photosphere. Magnetic flux emergence present as a dipolar feature appeared in pairs or a unipolar feature emerged inside a region dominated by opposite-polarity fields. Correspondingly, the reverse process is called magnetic flux cancellation. Both of them are likely to lead a magnetic reconnection but not necessary. On one hand, the direction of flux emergence can bring parallel or anti-parallel configuration to the existing fields. On the other hand, the flux cancellation can be products with different essence, such as converging flow with single or multiple loop system (Figure 1.6).

The relation between all these small-scale dynamics, especially across different layers in the solar atmosphere is under active investigation. Many studies find evidences that activities in the upper atmosphere have associated photospheric

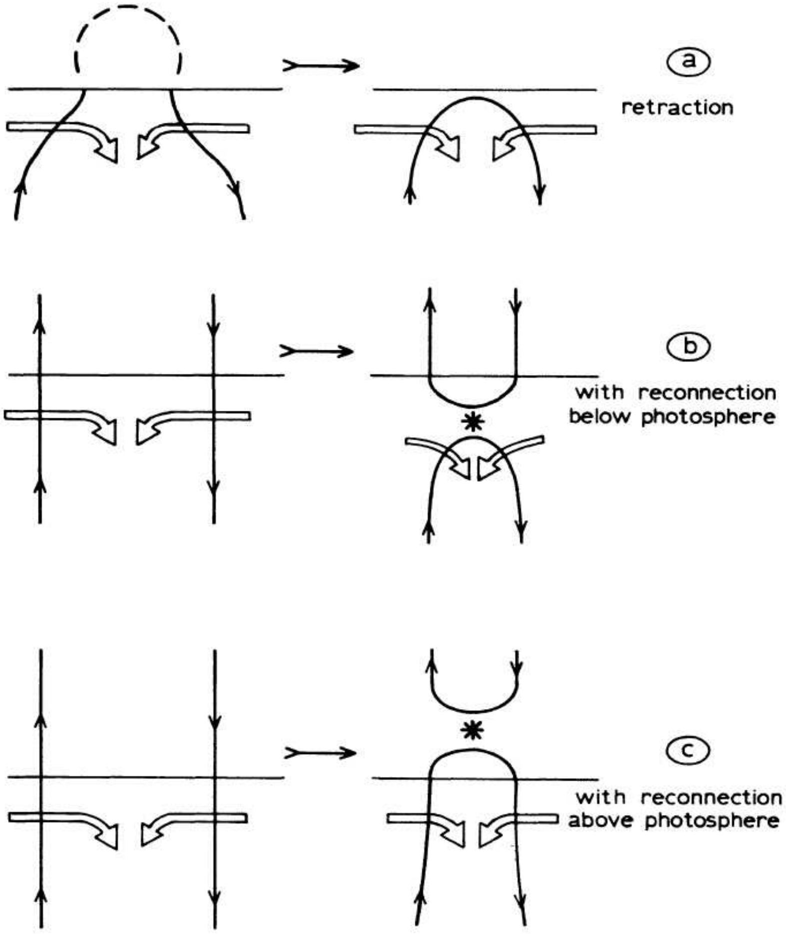

Figure 1.6 Schematic of magnetic flux cancellation in three different scenarios. The broad open arrows indicate the converging flows in the photosphere (horizontal lines), thin lines with arrows are magnetic field lines and asterisks show the sites of magnetic reconnections (Zwaan 1987).

magnetic field evolution, although they are not as obvious as flares in active regions (Figure 1.7). Small scale magnetic reconnections are conceivable driving mechanism of these activities. However, they may not follow the similar process with the standard flare model and currently there is no unified model for all small-scale activities.

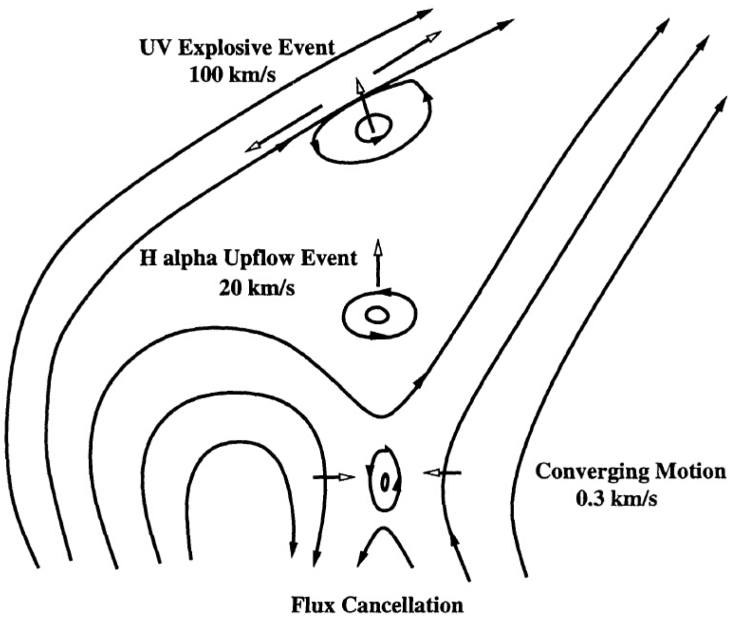

Figure 1.7 Schematic of a model of Chae (1999). It shows magnetic flux cancellation, Hα upflow events and transition region explosive events all relate to magnetic reconnections driven by the converging motion.

1.5 Scientific Goals and Dissertation Outline

In recent years, the considerable advances of instruments for solar observation provide an excellent opportunity of new discoveries in solar physics. As outlined above, the studies of small-scale dynamics thirst for high spatial, high temporal and high spectral resolution observations in order to resolve these tiny and transient processes. Besides improved resolutions, round-the-clock observations with comprehensive wavelengths also contribute to the studies of flares and CMEs. The modern observations include those from state-of-the-art telescopes, such as Solar Dynamic Observatory (SDO) and Interface Region Imaging Spectrograph (IRIS) in the space, as well as Big Bear Solar Observatory (BBSO) and National Solar Observatory (NSO) as ground-based facilities.

The scientific goals of this dissertation are divided into small-scale and large-scale dynamics associated with the magnetic reconnections. For large-scale flare study, it is to further explore the process of magnetic reconnection, especially the structure of current sheets. With the aid of new instruments, this study contributes to observational constraints for flare modeling. For small-scale dynamics, a statistical study would be able to generalize more detailed properties of events and reveal the possible relation among different wavelengths and magnetic fields. By taking the advantage of advanced data mining tools in addition to the high quality data, this study may further contribute to the coronal heating problem.

The context of this dissertation is arranged as follows:

- Chapter 1: Introduction. The first chapter presents an overview of the major aspects in solar physics (Section 1.1), the solar atmosphere (Section 1.2), the magnetism of the Sun (Section 1.3) and solar activities in large scales especially flares (Section 1.4.1), as well as various small-scale dynamics (Section 1.4.2).
- Chapter 2: Data Source. This chapter introduces several ground and space based instruments and their characteristics, which provide the data for both small-scale and large-scale studies in this dissertation.
- Chapter 3: Development of Data Analysis Tools. This chapter illustrates feature tracking methods used in studies of small-scale dynamics and specific tracking tools developed by me (published in *Research in Astronomy and Astrophysics*, 15, 1012, 2015) for magnetic flux cancellations (Section 3.2) and

RBEs (Section 3.3). In addition, for large-scale studies, we utilize the differential emission measure (DEM) analysis which will be introduced in Section 3.4.

- Chapter 4: The Statistical Study of Rapid Blueshifted Excursions and Magnetic Field Evolution. This chapter relates to the studies of small-scale dynamics. We employ our specific tracking tools in the coordinated observation to detect RBEs and magnetic flux cancellations. Their statistical properties are generalized and we further discussed the relationship between them. (This chapter is based on the following papers: Chen, Xin; Deng, Na; Lamb, Derek A.; Jing, Ju; Liu, Chang; Liu, Rui; Park, Sung-Hong; Wang, Haimin, *Research in Astronomy and Astrophysics*, 15, 1012, 2015, and Deng, Na; Chen, Xin; Liu, Chang; Jing, Ju; Tritschler, Alexandra; Reardon, Kevin P.; Lamb, Derek A.; Deforest Craig E.; Denker, Carsten; Wang, Shuo; Liu, Rui; Wang, Haimin, *The Astrophysical Journal*, 799, 219, 2015)

- Chapter 5: Thermodynamics of Supra-Arcade Downflows (SADs) in Solar Flares. This Chapter presents SAD observations which related to the current sheet in the large-scale dynamics. Using DEM analysis to diagnose their thermal properties, we demonstrate SADs are indeed void, i.e., they contribute negligible DEM, which is against to most of existing models. (This chapter is based on the following paper: Chen, Xin; Liu, Rui; Deng, Na; Wang, Haimin, ready to submit, 2016)

- Chapter 6: Summary of the Dissertation and Future Perspectives.

CHAPTER 2

DATA SOURCES

2.1 NSO/DST/IBIS

Dunn Solar Telescope (DST) of the NSO (Sacramento Peak, NM, USA; Zirker 1998) is a solar tower which has observed the sun using its 76 cm aperture for nearly half a century. The Interferometric BIdimensional Spectrometer (IBIS; Cavallini 2006) was completely installed in June 2003 on the DST, which provides its powerful spectral analyzing ability to DST with its key components, a series of two Fabry-Pérot interferometers. For our small scale study, it is necessary to acquire high quality data sets of chromospheric spectral lines that obtained by the coordinated observations using both IBIS and *Hinode* (Section 2.2). Spectral images and magnetograms have been successfully obtained in fall of 2011 & 2012 with myself participated in observations at NSO/DST. IBIS brought spectral imaging scans with 0.1 Å intervals, about $0\farcs1$ per pixel image scale and 6.3 frames s^{-1}. The field of view (FOV) is about $100'' \times 100''$ (a circle with a diameter of $96''$). Nowadays, for ground based observations, adaptive optic (AO) is important to improve the preference of large aperture telescope since the existing of the seeing. During the observations, with the 76-subapertures AO system working all the time, the seeing is mainly moderate with some good periods which provide the most valuable data for analysis.

2.2 Hinode

The *Hinode* mission is launched in September 2006. It carries three instruments which focus on different wavelengths: the Solar Optical Telescope (SOT; Tsuneta et al. 2008), the Extreme Ultraviolet Imaging Spectrometer (EIS) and the X-ray Telescope (XRT). The SOT is especially important for this study because it provides high quality magnetograms using its sub-systems, the Narrowband Filter Imager (NFI) and the Spectropolarimeter (SP). The NFI provides polarimetric images for several spectral lines. Some of them are sensitive to the Zeeman effect (MgI b, NaD etc.). In the coordinated observations, NFI simultaneously observed magnetograms with high spatial resolution and high cadence (about 64 s) for the same target regions as IBIS. The image scale of those magnetograms is $0\overset{\prime\prime}{.}16$ per pixel and the FOV is $131'' \times 123''$. By carefully coordinating the pointings of DST and *Hinode*, excellent overlap of both FOVs are obtained. As a supplement, the SP observations can provide a spectral diagnosis at a relatively low cadence, in view of high precision full Stokes polarimetric information.

2.3 SDO/AIA

Since the launch of SDO (Pesnell et al. 2012) in February 2010, it has become a key observing facility for solar physicists. In particular, the Atmospheric Imaging Assembly (AIA; Lemen et al. 2012) on SDO is revealing an unprecedented view of the solar corona as designed. It can reach $1''$ resolution with a full-disk view simultaneously for 10 EUV and UV passbands at a cadence of 12 s. With the aid of its state-of-the-art imaging ability, more and more details of the solar corona especially the flaring region have been discovered. In addition, new research methods have become feasible or effective such as the DEM method. Besides AIA, the Helioseismic and Magnetic Imager (HMI) provides full-disk, both line-of-sight (LOS) and vector magnetograms of the sun with the same resolution as AIA. The third instrument is Extreme Ultraviolet Variability Experiment (EVE), measures the solar total EUV irradiance and the corresponding variance as a star.

CHAPTER 3

DEVELOPMENT OF DATA ANALYSIS TOOLS

3.1 Introduction

The high quality data obtained from state-of-the-art instruments indicate the importance of data mining tools. Especially for the small-scale dynamics in this study, we focus on the Rapid Blueshifted Excursions and possibly associated magnetic flux cancellations (see Section 1.4.2), which both are highly frequent and transient features. To detect them and study their properties, corresponded feature tracking methods are necessary. In this section, we introduce capability and limitation of the present methods and illustrate the new specified tools developed by me for RBEs (Section 3.3) and flux cancellations (Section 3.2), respectively. In addition, the definition of DEM and the application of this method are presented in the Section 3.4 which related to the large-scale dynamics in this study.

To study the properties of the numerous small-scale dynamic features like RBEs, an appropriate detecting and tracking method would be important. Since RBEs are tiny (few arcseconds) and ephemeral and display diverse spectral profiles, detecting them requires observations with high spatial, temporal, and spectral resolution. There is an automatic algorithm developed for the RBE studies (Rouppe van der Voort et al. 2009; Sekse et al. 2012), which is designed for observations taken by the Crisp Imaging Spectropolarimeter at the Swedish Solar Telescope on La Palma. It combines different methods to detect RBEs, such as using Doppler images derived from the difference between the blue- and red-wing images, and using the extreme far bluewing image as a reference to eliminate background. This algorithm requires multi-frames restoration of images as well as excellent seeing; otherwise, the mismatch of features in different wavelengths would induce many false-positive detections during subtraction. In this study, we develop a new automatic RBEs tracking algorithm, which has a better tolerance of minor mismatches induced by image distortions or occasional seeing variations. Moreover, when the nearly simultaneous photospheric magnetograms are available, our tool as described below provides properties of RBEs and the comparison results with their associated photospheric magnetic features.

In order to study the magnetic configuration and evolution related to RBEs, we take the advantage of a well-developed and widely used solar magnetic field tracking method, the Southwest Automatic Magnetic Identification Suite (SWAMIS; DeForest et al. 2007), which can track weak-field features close to the noise level. Applying SWAMIS to LOS magnetograms taken by the Michelson Doppler Imager on board the *Solar and Heliospheric Observatory* and *Hinode*/SOT, Lamb et al. (2008, 2010) demonstrated one kind of observational effect: sometimes the apparent unipolar magnetic flux emergence is actually the coalescence of tiny, previously existing fluxes, which can be observed in higher resolution. Recently, they also found a similar process when unipolar magnetic features disappear (Lamb et al. 2013), meaning that the dispersal of flux concentrations might play a more important role than bipolar cancellations in the quiet Sun. However, we found that SWAMIS is likely to miss many cancellations under certain conditions, especially when the sizes of canceling features are significantly different. In order to better detect and characterize the photospheric magnetic cancellation, we thus developed an algorithm that specializes in tracking cancellations using the intermediate results of SWAMIS. The location and timing of the detected flux cancellations can then be compared with those of the detected RBEs.

3.2 Tracking Photospheric Magnetic Features

To study the small-scale magnetic flux cancellations, it is necessary to develop and utilize an appropriate detecting method. For the magnetograms in the coordinated observation, the main goal is to find flux cancellations of a similar scale to RBEs in chromosphere. In principle, flux cancellations are manifested as a reduction of net flux of the adjacent opposite-polarity features. Detecting them requires a tool that is capable of accurately characterizing small-scale magnetic elements in the weak field regions, such as quiet Sun and coronal holes. As mentioned in Section 3.1, SWAMIS has demonstrated to be able to automatically track magnetic features close to the noise level (DeForest et al. 2007).

As a brief introduction, SWAMIS works in five steps on data that has typically been preprocessed to reduce the noise floor and remove perspective effects:

(1) Discrimination: for each frame, determine regions of potential features;

(2) Identification: for each frame, index potential features in marked regions;

(3) Association: connect features across different frames;

(4) Filtering based on size/longevity: remove occasional cluster of noise;

(5) Classification of origin and demise (DeForest et al. 2007).

As a result, SWAMIS provides properties of each magnetic feature in each frame (flux, area, location), and summary information for each feature (birth and death times and the ways of birth and death).

After a careful investigation, we found that SWAMIS often misses cancellations in a particular situation, when the cancellation occurs between two opposite-polarity features with significantly different sizes. In this case, one magnetic feature has considerably more unsigned flux than the other. During such a cancellation event, the larger feature could even show an increase of unsigned flux due to random noise accumulated within the extended area, or due to its simultaneous merger with other like-polarity features. This presents a challenge to SWAMIS, as it tests the flux balance to confirm a cancellation event, under the assumption that the unsigned flux would decrease for both features involved as in a standard flux cancellation. As a consequence, this kind of cancellations would be classified as "Error" by SWAMIS rather than "Cancellation" because of the apparently unbalanced change in flux. In addition, SWAMIS only checks the status of both features when either of them dies out. But sometimes a cancellation event does not entirely eliminate either features; both of them just become weaker and smaller, and then separate from each other. Since both features still exist, SWAMIS would not check their status and consequently would miss these cancellations. For the difficulties mentioned above, we made our cancellation tracking tool mainly by amending the corresponding portion in the original SWAMIS algorithm in two aspects. First, the size ratio of canceling features is now considered in order to define the confidence of their fluxes (see below).

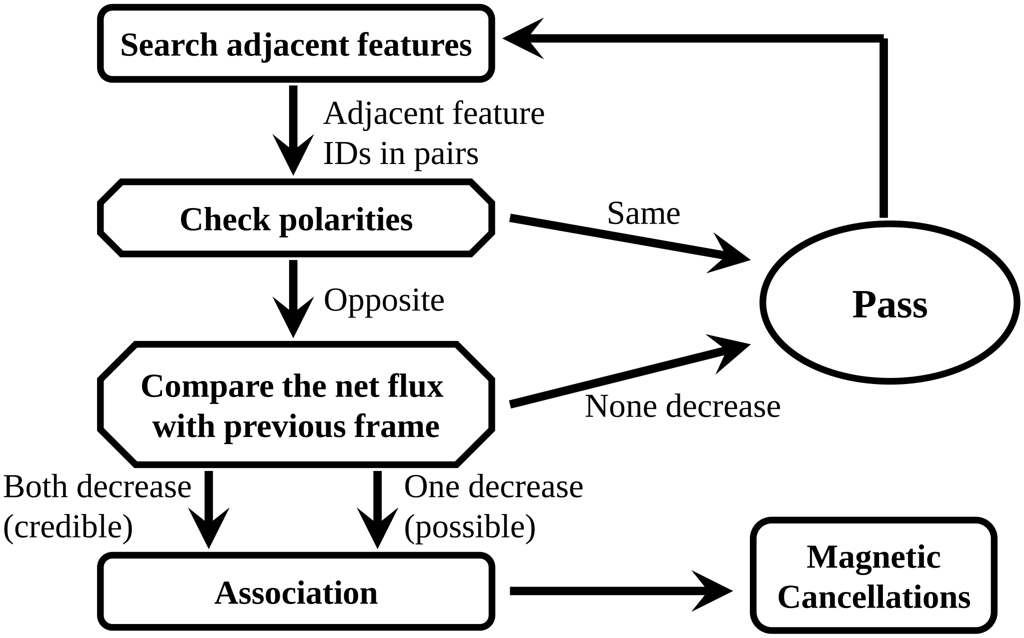

Figure 3.1 Workflow of tracking magnetic cancellation using a modified code based on SWAMIS.

Second, the cancellation is no longer treated as the demise of magnetic elements but is monitored during the whole lifetime of the involved features.

In practice, our procedure of tracking magnetic cancellation is described as follows. We first apply the original SWAMIS code to detect magnetic features following the method in Lamb et al. (2010). In preprocessing, the data are calibrated, carefully aligned, and spatially and temporally smoothed using Gaussian kernels (see Section 4.2). Based on the noise level, image resolution, and data cadence, we then set appropriate thresholds of feature intensity, size, and lifetime. The result of SWAMIS contains the properties of each detected magnetic feature, such as location, flux, and size. These properties from results of SWAMIS are extracted and fed as input to our cancellation tracking tool, which includes the following main steps (Figure 3.1):

i) For each frame, search adjacent features (i.e., separated less than 3 pixels, $0.5''$) and return their ID in pairs;

ii) Check the polarities of each pair, and remove pairs with the same polarity;

iii) Check the change of net flux of each feature by comparing its unsigned flux in the current frame with that of the previous frame. Record the credibility of cancellation as “credible” (if the unsigned fluxes of both features in a pair decrease), “possible” (if the unsigned flux of only one feature in a pair decreases), or “impossible” (if no feature in a pair exhibits a decrease of the unsigned flux). The pairs labeled with “impossible” are removed;

iv) Associate cancellations across different frames in the magnetogram sequence.

The result of our cancellation tracking tool contains analysis of credibility in addition to the general characteristics like flux variation, location, birthtime and deathtime. Quantitatively, in step iii), the “credible” cases have a credibility of 1 and “impossible” cases correspond to a zero. Those “possible” cases have their credibility ranging from 0.25 to 0.75, based on the ratio of sizes (i.e., area) of features. Specifically, as mentioned above, the total flux of a larger feature has a larger absolute uncertainty. For example, if the feature with increased unsigned flux (UF, same-below) is significantly larger (e.g., twice or larger) in size than the other feature with decreased UF, the credibility is set to be 0.75. Similarly, if the UF of larger feature decreases while that of the smaller one increases, the credibility is set to be 0.25. If both features have a similar size, the credibility is set to be 0.5. For each cancellation, the credibility is evaluated in each frame, and the mean value averaged over all frames in which cancellation sustained is used as the final credibility.

Our specialized cancellation tracking tool shows an improvement of detection and also provides more accurate space-time information. Specifically, first it shows a better capability to find cancellations that involve features of different sizes. Using our tool, the flux uncertainty of a large feature would lead to a lower credibility rather than an error, which is more quantitative. Rather than merely checking the last few frames of canceling features, our algorithm thus exploits more information from the data to provide a trustworthy result. Second, our algorithm directly shows the location and initiation time of cancellations, which can not be obtained by SWAMIS as it focuses on magnetic features themselves. For example, central coordinates of the involved magnetic features may not appropriately indicate the cancellation site, when the features have relatively large sizes or irregular shapes. Similarly, the birth time of the involved magnetic features is generally earlier than the onset of cancellations. By handling cancellations as associated events, our tool can provide accurate location and time range information of cancellations. Finally, we find that sometimes both features of opposite polarity do not totally cancel out. In general, during a cancellation event, the size of features as well as their unsigned fluxes would decrease. But it does happen that when features become smaller, their remaining parts move apart instead of toward each other. In fact, these features could merge with other features of like-polarity or disperse in situ, which are not identified as cancellations by SWAMIS but are recorded by our algorithm. In summary, our modified tool provides more comprehensive and accurate properties of magnetic cancellations.

3.3 Tracking Chromospheric RBEs

For RBEs, we developed a corresponding automatic tracking method for the four-dimensional (x, y, t, and λ) data cube observed by IBIS. The task becomes more complicated due to the presence of the spectral dimension. To facilitate the data analysis and achieve our goal, it seems desirable to "compress" the wavelength information thus remove the spectral dimension by, for example, making a Doppler map. However, Doppler maps can not be utilized directly by subtracting the difference between the blue- and red-wing images due to the distortions of IBIS images at different times. Besides, there is a scenario that RBEs may partially overlapped with individual features on the red-wing, e.g., Rapid Redshifted Excursions (RREs; Sekse et al. 2013b) in spatial or in temporal, which would make it not appropriate to use Doppler maps (the blue-shifted component and red-shifted component would cancel each other). we notice that histograms of line-wing images are "unbalanced", i.e., it is a superposition of chromospheric flows which manifest as absorptions and the photospheric image which is gaussian-like histograms in the quiet sun. Based on the unbalanced histogram as well as the noise level, we try to calculate a threshold for detecting Doppler-shifted regions in the images of each different spectral position. However, this threshold can not distinguish the photospheric background features at far wings, such as granule boundaries. These are the main issues need to be resolved.

In order to properly process the spectral information, our method tries to extract the contrast profile for each pixel with several corrections. Using this contrast profile we can calculate the Doppler velocity and detect RBEs. Our method is described as follows.

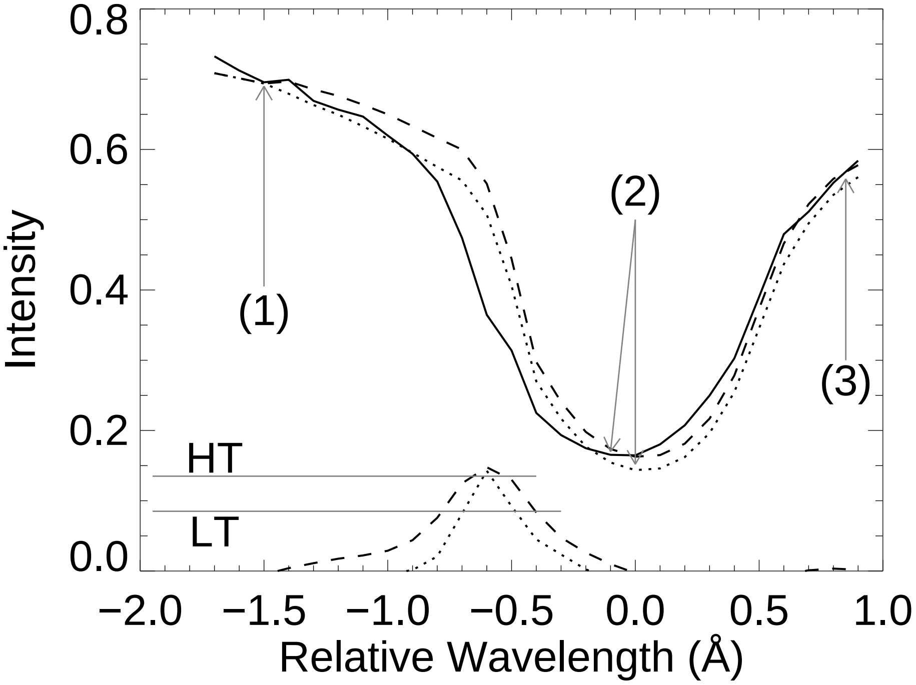

Figure 3.2 Illustration of normalized reference profile and dual-threshold method. The solid line is the line profile of an arbitrary pixel (local profile). The average profile (dotted line) is multiplied by a scaling factor $f(\lambda)$ to construct the normalized reference profile (dashed line) which has the same intensity of local profile at far blue wing (1), line minimum (2), and far red wing (3). The scaling factor $f(\lambda)$ between points (1)-(2)-(3) is interpolated in order to keep the shape of reference profile. Contrast profiles are plotted at the bottom. The dotted line is derived by the average profile and the dashed line is derived by the normalized reference profile. The horizontal gray lines indicate the high threshold (HT) and low threshold (LT). As an example, this pixel passes the high threshold.

First, we normalize reference profiles over the entire FOV to remove the background features. Specifically, rather than using the average profile of the whole FOV as the reference, for each pixel, we scale the average profile to match the local profile but keep the line core unshifted, as illustrated in Figure 3.2. A normalization procedure keeps reference profiles in a similar shape, and allows intensity to vary in different locations to reflect background features (especially at far wings). In other words, normalized reference profiles simulate a profile which has no shifted spectral component at the same local background. In this way, contrast profiles with most of the background features removed can be constructed (using normalized reference profile minus local profile).

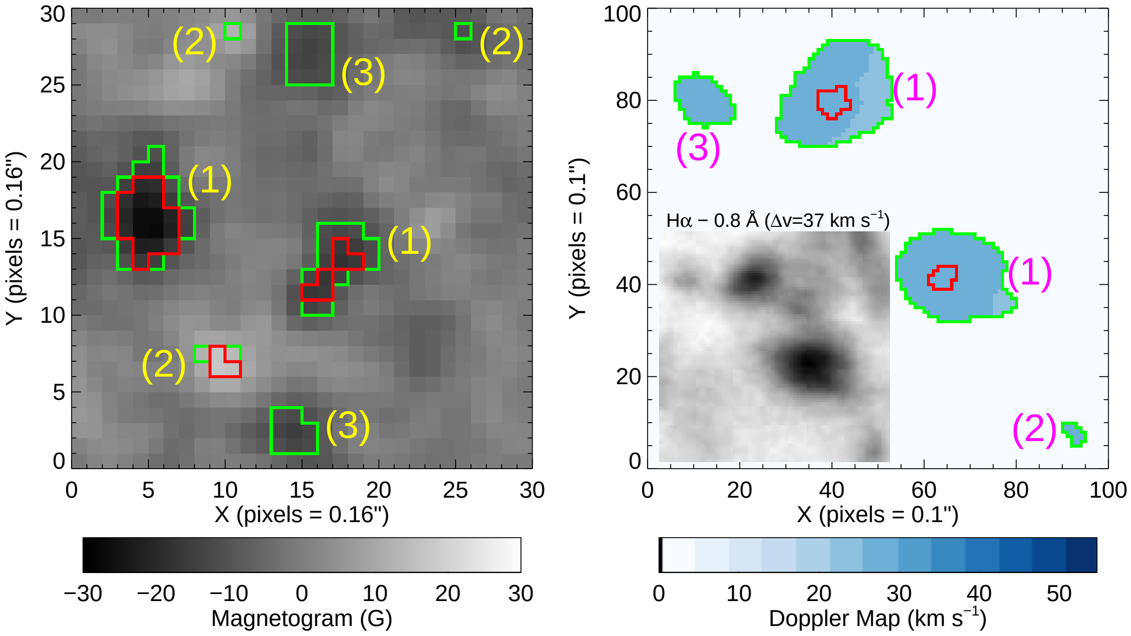

Figure 3.3 Illustration of dual-threshold method used for tracking magnetic features (left) and RBEs (right). For both panels, the red contours show the high threshold and the green contours correspond to the low threshold. Features labeled (1) have pixels that exceed the high threshold in the current frame; features labeled (2) are small and likely to be filtered out if they are not bigger in some previous or subsequent frame; features labeled (3) are large enough to avoid size-based filtering, do not have any pixels that exceed the high threshold in the current frame, but do have some pixels that exceed the high threshold in some previous or subsequent frame. For the 4D spectral data, we applied the dual-threshold method to the intensity of contrast profiles (see Figure 3.2), which are not shown in the Doppler map (in contrast, thresholds can be directly presented as contours in magnetograms). In the right panel, the insert is an H$\alpha - 0.8$ Å image corresponding to this Doppler map (at the same time and location). This gives an intuitive but incomplete view reflecting those thresholds, as only one line position instead of the whole bluewing of Hα is presented in the figure.

Second, to account for the image distortion, we do a spatial smoothing of images as the multi-frame restoration is not available for our IBIS observations. The spatial smoothing process could reduce the noise but it decreases the image resolution as well. For our data set, although the noise level is very low, the distortion is similar to sporadic noise that can be reduced by spatial smoothing. Since the pixel size of IBIS images is much smaller than the resolution, spatial smoothing would in fact not decrease the real resolution of our data set. In addition, as IBIS observation has high spectral resolution, our data set mostly shows a continuous spectral profile. This indicates that any discontinuity, especially the step-like structure in the spectral profile, could be due to a mismatch of pixels in different wavelengths. Therefore, we also apply a smoothing procedure to the contrast profile in the spectral dimension. Both the spatial and spectral smoothing can effectively reduce the false-positive detections.

Finally, our method utilizes a dual-threshold method to improve accuracy (Figure 3.3). For solar magnetic field tracking, the dual-threshold method as used by SWAMIS has the advantage in the discrimination of features (DeForest et al. 2007). In its implementation, the high threshold is used to mark the desired pixels, while the low threshold is only applied to pixels that are adjacent to the marked ones. By properly determining both thresholds based on the noise level, this method performs better than detections using a single threshold. However, for the RBE tracking, we can not directly apply this dual-threshold approach to the 4D data cube. For magnetograms, as each pixel has a value that is a superposition of signals (if valid) and noise, the dual-threshold method can effectively extract the LOS magnetic field signal after filtering out the pure noise. While for the Hα data, each pixel has a line profile instead of a single value. We found that the noise mainly affects the intensity of contrast profiles, but the signal of our interest is the Doppler shift shown in the contrast profile. Therefore, our tool is designed to apply the dual-threshold method to the intensity of contrast profiles, and extract Doppler velocities rather than the intensity of interested regions. As a result, our tool constructs a series of marked 3D Doppler maps. These maps are ready for the subsequent feature tracking, which is similar to SWAMIS.

In summary, our RBEs/RREs tracking method is carried out as follows:

i) Pre-process the data, including calibration, alignment, bad frame correction, and spatial smoothing;

ii) Construct a normalized reference profile for each pixel, and obtain contrast profiles;

iii) Apply the dual-threshold feature discrimination algorithm on contrast profiles, and create Doppler velocity maps that are marked with confidence level information;

iv) Employ the general feature tracking procedure, including feature identification and association etc.

It is worth mentioning that different from magnetic features that have either positive or negative polarity, the RBEs and RREs may be overlapped at the same time and location. Thus, our method tracks the blue wing for RBEs and the red wing for RREs, separately. Our tracking tool records the properties of each detected

RBE/RRE, such as central location, shape, horizontal length, and Doppler velocity in each frame during their lifetime.

3.4 Differential Emission Measure

In the corona, analysis of plasma properties such as density and temperature is crucial to understand the mechanism of solar activities through observations. It is common that a coronal source shows response in multiple wavelengths corresponding to different temperature ranges. On one hand, it must be aware that corona is optically thin in EUV and SXR wavelengths, thus, the observations does not only represent local plasma but also integrate along the line of sight. On the other hand, considering the transport of coronal plasma in restrained by magnetic fields in most scenarios, i.e., each flux loop is isolated with adjacent ones. Therefore, for coronal plasma in arbitrary limited space, the multi-temperature distribution is appropriate description that presents components of different temperature weighted by the corresponding plasma density.

Generally, in the optically thin solar corona, the emission measure (EM) is proportional to the square of electron density in a certain volume. Accordingly, as a quantitative expression of the multi-temperature distribution, DEM can be written as

$$DEM(T) = n_e^2(h)\frac{dh}{dT}, \tag{3.1}$$

where n_e is the electron density at temperature T at the position coordinate h along the line-of-sight. The observed signal in the ith channel, g_i, is related with DEM by

$$g_i = \int_T K_i(T) DEM(T) dT + \delta g_i, \tag{3.2}$$

where $K_i(T)$ is the temperature response of the ith channel and δg_i is the corresponding measurement error. Although to recover DEM based on the observed data and instrumental parameters is feasible, it is a well-known ill-posed inverse problem. Solve this problem through direct inversion would lead a rapid growth of measurement error. Thus, the main difficulty of this problem is to constrain the uncertainty, which has been attempted by several different methods. One approach is applying a presumed model in addition to solve DEM, e.g., with discretised spline model (Weber et al. 2004) or multiple Gaussian model (Aschwanden & Boerner 2011). These methods have been utilized in several studies, however, they are computationally slow and their results rely on the compatibility of the presumed models. There are several other methods without using a presumed model but different algorithm, which each has its own advantages and disadvantages.

The method we used to reconstruct DEM in the large-scale dynamics of this study is an enhanced regularization method newly developed by Hannah & Kontar (2012). It has been employed to analyze several events (e.g., Hannah & Kontar 2013; Chen et al. 2014; Gou et al. 2015). This code calculated DEM using the six AIA EUV channels. The results yield DEM for each individual pixel, its uncertainty, and the temperature resolution. This method is computationally fast and by taking this advantage it is feasible to provide the DEM maps for massive data. Moreover, it also provides the horizontal uncertainty (temperature resolution) which is absent in most of the other methods.

CHAPTER 4

THE STATISTICAL STUDY OF RAPID BLUESHIFTED EXCURSIONS AND MAGNETIC FIELD EVOLUTION

4.1 Introduction

Observations of small-scale dynamics in the chromosphere have benefited from significant improvements in instrumentation in the past decade. In the earlier on-disk Hα observations, one kind of small-scale feature was discovered to show blue-shifted (upflow) component only with no corresponding red-shifted (downflow) component. They were named H$\alpha - 1.0$ Å jets (Wang et al. 1998) or chromospheric upflow events (Chae et al. 1998; Lee et al. 2000). It was found that these jets tend to occur at supergranular boundaries, and sometimes recur on the same sites. They mostly appear to be round in shape rather than elongated. More recently, when observed at the solar limb, the highly dynamical type II spicules were distinguished by their outward-only ejection, high speed ($15 \sim 40$ km s^{-1}), and short lifetime (< 150 s) comparing to the "classical" type I spicules (De Pontieu et al. 2007). Later, these type II spicules were linked to their on-disk counterparts, the Rapid Blueshifted Excursions (RBEs; Langangen et al. 2008; Rouppe van der Voort et al. 2009), which are essentially similar to the upflow events mentioned above.

Using observations with improved resolution, more detailed properties of RBEs were revealed. Statistically, their occurrence rate is compatible with that of the type II spicules (Rouppe van der Voort et al. 2009; Sekse et al. 2012). In addition, RBEs are mostly elongated and their upflows are accelerated from the footpoint to the top end.

Although they have been known separately in Hα and Ca II 8542 Å observations for several years, new studies show that their positions and accelerations exhibit consistency from the lower layer (Ca II) to the higher layer (Hα) of the chromosphere (e.g., Sekse et al. 2012). Sometimes, this connection can also be extended to corona to appear as bright points according to observations made by AIA on board SDO (De Pontieu et al. 2011). Besides the upflow motion along LOS, RBEs also show transversal and torsional motions (Sekse et al. 2013b), which are of comparable magnitude to the type II spicules (De Pontieu et al. 2012). Furthermore, features in the red wing but with similar characteristics to RBEs were discovered and named Rapid Redshifted Excursions (RREs; Sekse et al. 2013b). It was found that RREs appear less frequent than RBEs, especially near the disk center. A significant fraction of RREs occur together with RBEs, which is interpreted by Sekse et al. (2013b) as being due to the upflow, transverse, and torsional motions in combination with certain viewing angles.

As almost all solar activities are related to the magnetic field, the magnetic configuration and dynamics associated with RBEs have been investigated in many studies. It is known that even in the quiet-Sun region, the magnetic field is not tranquil but has dynamic network and intra-network structures. As mentioned previously, RBEs tend to occur near the concentration of photospheric magnetic field, and are sometimes associated with converging magnetic dipoles (Wang et al. 1998). Considering their highly dynamic characteristics, RBEs may be propelled by small-scale magnetic reconnection. In this case, magnetic cancellations are likely to indicate the source locations of RBEs. On the other hand, using the three-dimensional

(3D) MHD simulations, Martínez-Sykora et al. (2011) showed that small-scale flux emergence would trigger a chromospheric jet similar to type II spicules. The plasma in the chromosphere can be heated and accelerated by a strong, mostly horizontal Lorentz force and is then ejected along the vertical magnetic field. Correspondingly, there is a case study showing that RBEs are related to the newly appeared magnetic flux concentrations (Yurchyshyn et al. 2013). However, the flux emergence and cancellation are likely to associate with each other. When new flux concentrations emerge from the bottom of the photosphere, they may cancel with opposite polarity fields in the vicinity. Thus far, although the importance of the RBE-associated magnetic field evolution has been generally recognized, the driving mechanism of RBEs is still under active investigation.

4.2 Data Processing

We employ our tracking tools to the coordinated observations of photospheric LOS magnetograms and chromospheric Hα spectral images, as introduced in Chapter 2. In this study, the 1 hr period observation is selected at a quiet-Sun region near the disk center(14:30-15:30 UT on 2011 October 21), when the seeing is relatively better and more stable than the other time periods during the observing run. For Hα observation, each scan contains 28 points between -1.7 Å to $+1.0$ Å relative to 6562.8 Å, and for Ca II, it contains 34 points from 8540.2 Å to 8543.5 Å. Besides the spectral scans (narrowband channel), synchronous white-light (broadband channel) images are also obtained for alignment and calibration purposes (Cavallini 2006; Reardon & Cavallini 2008). As a result, the cadence for a full scan is 4–5 s for Hα and 5–6 s for Ca II using ~ 30 ms exposure time with $\sim$6 frames s^{-1}. In addition, in order to fully cover the evolution of magnetic features, we analyze the *Hinode*/NFI magnetograms in a wider 2 hr time window (14:00-16:00 UT on 2011 October 21).

A series of preprocessing are executed for both data sets and define proper thresholds. For magnetograms, we follow the steps as outlined in Section 3.2. Since NFI data were recorded by two CCD cameras, occasionally there is an offset between them, which is not removed by the standard calibration routine (`fg_prep.pro` in the solar software). To correct the offset, we use a linear compensation method refer to Lamb et al. (2010). However, there are still some bad frames that show a relatively larger shift of FOV than other frames. To cope with this situation, we first remove each bad frame manually and split the rest images into blocks. For each block, we then average all frames of that block and use it as a reference for alignment. Finally, we align all blocks to the middle block so that the whole image sequence is aligned. In addition, images are Gaussian-smoothed both temporally (using 5 frames) and spatially (using 3 pixels). After these smoothing, the noise level is about $\sigma = 5.5$ G, and we select $2\sigma = 11$ G and $3\sigma = 16.5$ G as the low and high thresholds of SWAMIS, respectively. We also configure SWAMIS to only track those features that are larger than 4 pixels ($\sim 0\overset{''}{.}1^2$) and appear more than 2 frames ($\sim$ 2 minutes) in order to minimize the false-positive detection.

For the IBIS spectral data set, the preprocessing follows a similar procedure as for the magnetogram data. First, we calibrate the data using the standard calibration routines for IBIS. After corrections for the dark and flat fields, each spectral scan is aligned and destretched with the aid of white-light images. The blue shift (especially at the edge of the FOV) induced by the collimated optical setup of IBIS is also compensated. Using a simulated pre-filter curve, we normalize the whole spectra based on the 1 hr data set. As mentioned in Section 3.3, each scan is spatially smoothed using a 3×3 Gaussian kernel ($\sigma = 1$) and the temporal smoothing is only used to replace bad frames. By checking the fluctuation in contrast profiles, we set the low (high) threshold to 9% (14%) absorption level. Finally, we convert the IBIS data set into continuous Doppler maps, and track RBEs and RREs separately using blue-wing and red-wing maps, respectively. Similar to the magnetic cancellation tracking, features smaller than 16 pixels ($\sim 0''.16^2$) or have a lifetime shorter than 2 frames (~ 10 s) are not included for study.

4.3 Statistical Results and Discussion

4.3.1 Statistical Tracking Result of Magnetic Cancellations

Using our cancellation tracking tool, a total of 2969 magnetic cancellation events are detected during the 2 hr NFI data. This result is further refined based on the credibility that considers the impact of the size and flux balance of features (i.e., credibility greater than 0.75, see Section 3.2). We realize that when tracking magnetic features close to the noise level, the flux of a feature could be quite uncertain as errors can accumulate from multiple pixels. Taking this into consideration, only 331 (11.1%) cancellations appear to reduce the unsigned flux of both positive and negative features during their entire lifetime. Nevertheless, our tool has the ability to identify a large number of possible cancellations and evaluate their credibility based on the surrounding magnetic configuration of features.

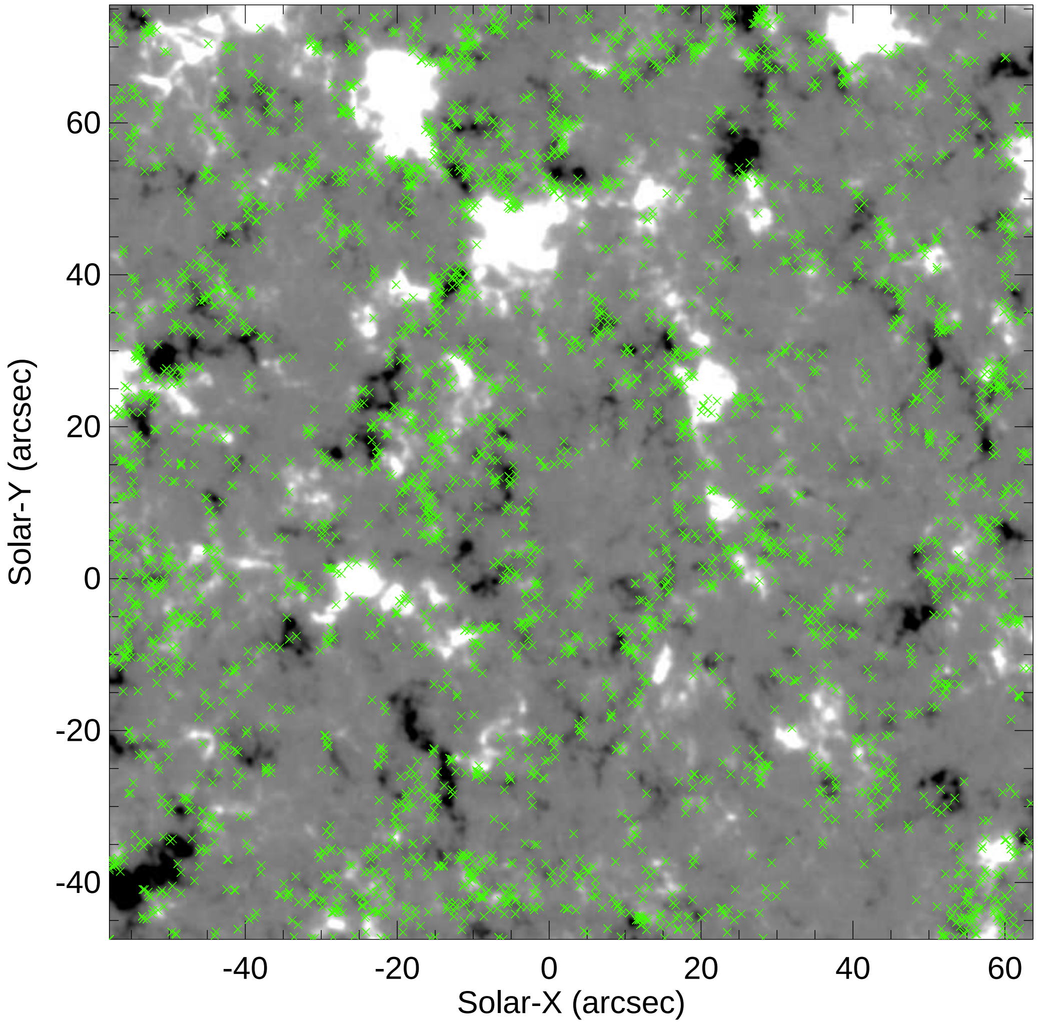

Figure 4.1 Detected sites of 2969 magnetic cancellation. The background is the average magnetogram in the 2 hr data set (scaled at ±50 G). Our tool tracks the adjacent segments from the border of each opposite-polarity feature and record the center of each pair of adjacent segments as the location of magnetic cancellation (shown as green crosses). Rather than using the middle point between the centers of canceling features, our method provides a more accurate location of cancellation involving a relatively large feature (center of a relatively large feature could be far away from the location of cancellation).

Accurate feature locating is another advantage of our cancellation tracking tool. Figure 4.1 shows the detected sites of cancellations (green crosses) superimposed on an average magnetogram. It is clear that the cancellations appear to outline the supergranular network as expected. This also implies that the credibility-level evaluation works as planned, in that highly credible cancellations appear at reasonable regions. Therefore, our tool can track more cancellations and pinpoint their accurate locations, and at the same time still minimizes the false-positive detection.

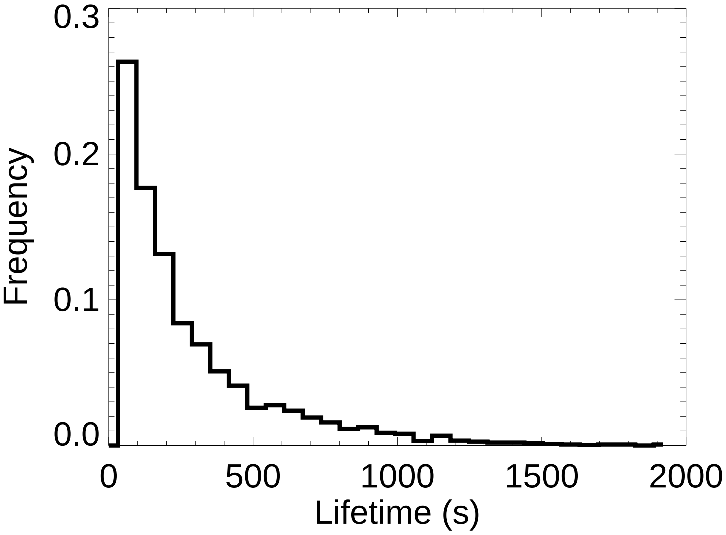

Figure 4.2 Histogram of lifetime of detected magnetic cancellations. The cadence of observation is about 64 s.

Based on the particular condition of the coordinated observation and the used thresholds, we statistically study the distribution of magnetic cancellations. The extrapolated occurrence rate of magnetic cancellation over the whole Sun is 80±33 s^{-1} ($1-\sigma$; 64 s cadence). As shown in Figure 4.2, the lifetime shows a monotonic decrease with a mean of 5 minutes. There are several studies analyze the flux cancellation rate in the photosphere (Chae et al. 2002; Park et al. 2009), however, it may not be appropriate for our study due to the following reason. Figure 4.3 shows the

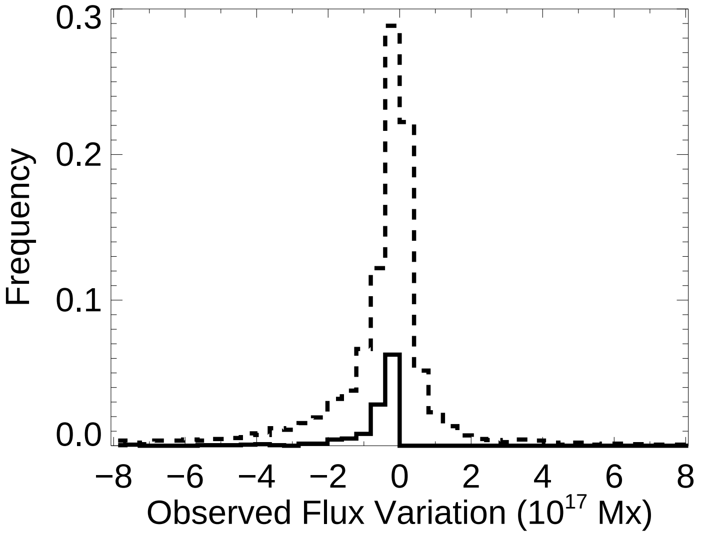

Figure 4.3 Histogram of the net flux (sum of the signed flux of both canceling features) of 2969 detected magnetic cancellations (dashed line) covering from birth frame to death frame of each event. The solid line shows the distribution of the most credible 331 cancellations (11.1%). One must be aware that the net flux variation depends on the feature size and is thus uncertain when tracking magnetic features close to the noise level.

distribution of the total net flux variation of both canceling features. Dissimilar to SWAMIS which relies more on this property, we note that there are some cancellations with high credibility that exhibit an increase of the total net flux. Although a magnetic cancellation is generally defined as a decrease of the total net flux, it can be easily misidentified due to the error of observation and detection. As mentioned in Section 3.2, we find that the size difference of canceling features plays an important role thus can not be ignored when checking the net flux balance. Figure 4.4 illustrates the different performances of SWAMIS and our modified tool.

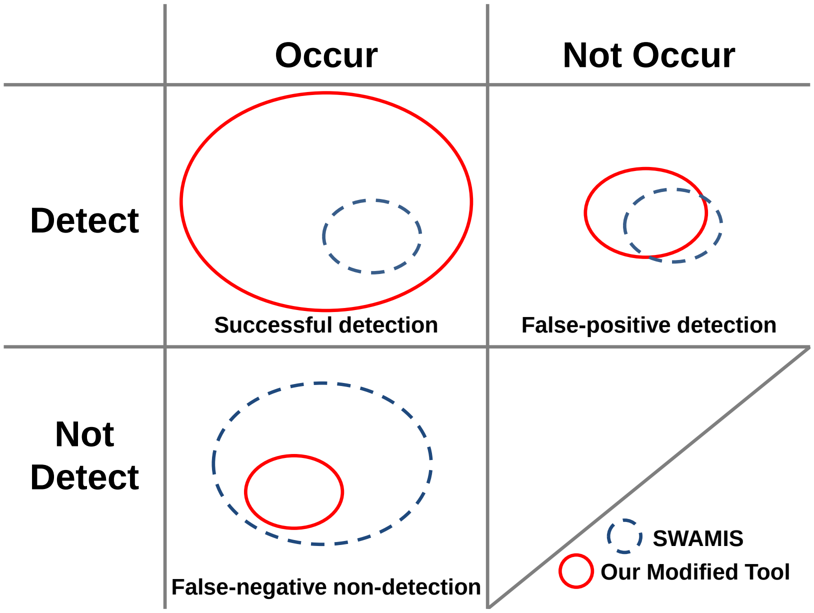

Figure 4.4 Contingency table of the performance of SWAMIS and our modified tool. Our modified tool detected much more (i.e., eight times) magnetic cancellation with a slightly lower (i.e., around 80%) credibility comparing to SWAMIS (using data set and thresholds mentioned in Section 4.2). In other words, our modified tool can significantly reduce false-negative non-detections and keep the false-positive detections in a similar level. Therefore, it provides a more comprehensive detection.

4.3.2 Statistical Tracking Result of RBEs

Using the 1 hr IBIS data set, we found 3022 RBEs that are not paired with RREs. Considering that an RBE is defined as a feature that shows no red-shifted component, we removed features detected from the blue wing, which are temporally and spatially associated or close to any feature detected from the red wing, as they could be the disk counterparts of type I spicules (with both upflow and downflow). Although Sekse et al. (2013b) interpreted this situation using a combination of transverse and torsional motions of RBEs under specific viewing angles, it is still under debate (Lipartito et al. 2014). In our data set, we hardly found any paired RBEs/RREs that are parallel to each other indicating a torsional tube of plasma.

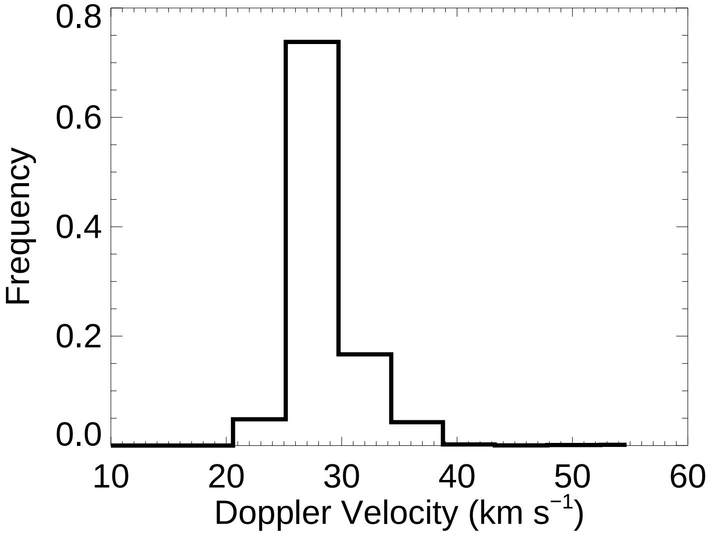

Figure 4.5 Histogram of Doppler velocity of detected RBEs. For each RBE, the peak velocity is presented during its lifetime.

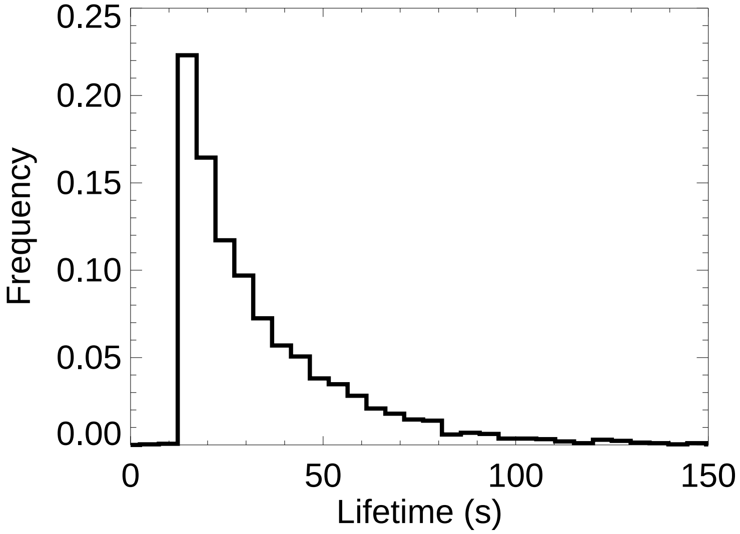

Figure 4.6 Histogram of the life time of detected RBEs. The data cadence is ∼4.85 s. The cut-off at ∼14.5 s (3 frames) is an artifact caused by our tracking method.

Figure 4.5 shows the histogram of Doppler velocity of the 3022 RBEs. The Doppler velocity mainly ranges from 20 to 40 km s^{-1} ($\sigma = 3.0$ km s^{-1}), with a mean

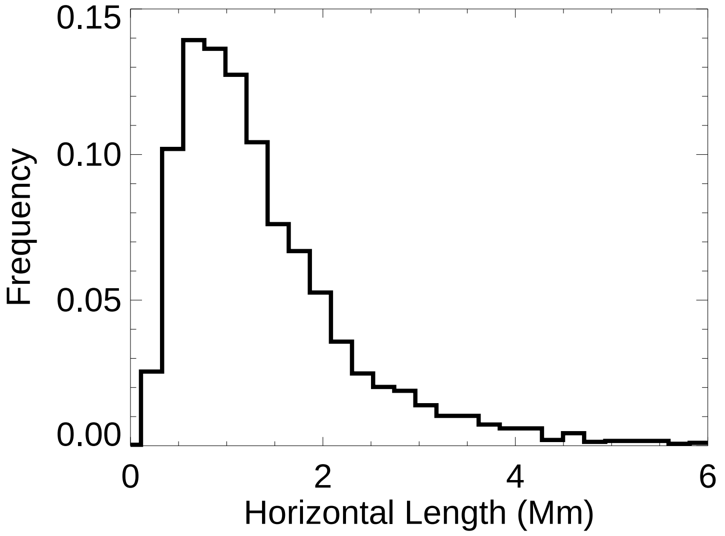

Figure 4.7 Histogram of the horizontal length of RBEs. The maximum length for each RBE is presented during its lifetime..

value of 28.5 km s^{-1}. This result is comparable to previous studies (Wang et al. 1998; Rouppe van der Voort et al. 2009; Sekse et al. 2013a) with a slightly higher mean velocity, which could be related to the different thresholds used. We note that there does not exist a clear cut-off Doppler velocity of RBEs, as also mentioned in Sekse et al. (2013a), since decreasing the detection threshold would lead to more RBEs. Taking advantage of the dual-threshold method that utilizes the whole spectral profile, our tool can reveal RBEs that has a low Doppler velocity but still exhibit a credible blue-shifted component. Furthermore, we find the lifetime of RBEs (Figure 4.6) is 35.2±27.5 s ($1 - \sigma$; data cadence is ∼5 s), as well as derive the occurrence rate of RBEs extrapolated to the whole Sun, which turn out to be 331±292 s^{-1}. These results agree with previous studies (Rouppe van der Voort et al. 2009; Sekse et al. 2013a). In addition, the horizontal length of the detected RBEs is found to be 1.50±0.96

Mm (Figure 4.7), and the shape of RBEs can be elongated (49%), round (22%), or irregular (29%). The RBEs in the coordinated observation are shorter in length and less elongated compared to previous studies mentioned above. This is probably due to the lack of the projection effect since the target region in our study is much closer to the disk center.

4.3.3 Relation Between RBEs and Magnetic Cancellations

Combining the tracking results of magnetic cancellations and RBEs, we attempt to look at the possible correlation between them using the coordinated observations. After a careful image alignment using the intensity images of NFI and white-light images of IBIS, Figure 4.8 presents the spatial distribution of the both identified features. It can be seen that the detected locations of magnetic cancellations and RBEs show some patterns rather than a uniform random distribution. As mentioned earlier, magnetic cancellations tend to concentrate on the magnetic network boundary, and indeed, most of them are surrounded by RBEs in our result as expected. Inside the network, magnetic cancellations are much less frequent. Accordingly, there are much less RBEs as well. In addition, there are several unipolar regions where many RBEs are present, but are lacking of magnetic cancellations.

As for the temporal association, out study is not yet to establish possible correlation in timing between RBEs and magnetic flux cancellation. Nevertheless, this does not imply that these two phenomena are totally independent of each other. In fact, we find that it could be technically difficult to examine the temporal correlation between them. Since RBEs occur frequently with a lifetime shorter than a minute

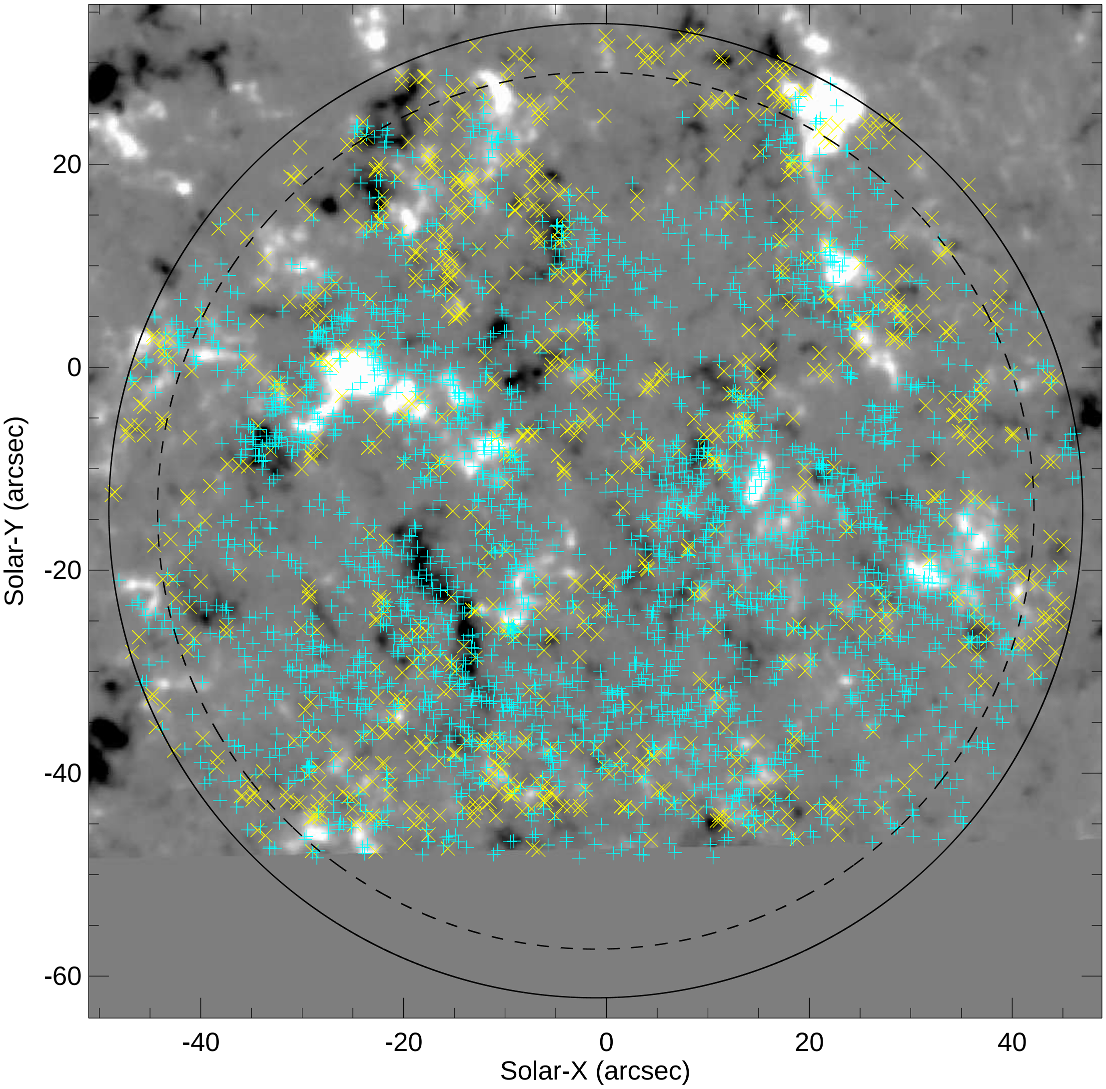

Figure 4.8 Spatial distributions of 936 detected magnetic cancellations (yellow crosses) and 2715 RBEs (cyan crosses), superimposed on an average magnetogram from 14:00 to 16:00 UT (scaled at ±50 G). The NFI magnetogram has been aligned with IBIS. The FOV of IBIS is denoted by the solid circle, while the dashed circle shows the central region with a 0.9 radius of the IBIS FOV. At the top edge of the IBIS FOV, RBEs are not identified due to a calibration problem.

and some magnetic cancellations could last 30 times longer than RBEs, it is always possible to apparently associate a nearby magnetic cancellation for a given RBE.

However, the intrinsic correlation between these two kinds of evolving features is still concealed which remains as a challenge. An approach utilizing these tools finds that the apparently spatiotemporal correlation between RBEs and magnetic flux cancellations are no better than random probability.

Finally, the statistical relation between magnetic cancellations and RBEs seems to be vague, as (1) both activities show a wide variety of their properties. (2) Both detection methods of cancellations and RBEs are not completely accurate, considering that either false-positive detection or false-negative non-detection may further increase the variance of their properties. (3) The confidence interval of correlation is more than a linear superposition of the variance of event properties. As a result, the confidence interval of correlation could easily become broad, which makes it less reliable. In this case, for example, even if every magnetic cancellation is related to an RBE, their correlation (either spatial or temporal) would not be close to 100% based on the detected features. To solve these problems, clearer definitions of magnetic cancellations and RBEs would be helpful, as they could reduce the variance of feature properties by limiting the samples themselves as well as increasing the accuracy of detection.

4.4 Summary

In summary, we have developed two automatic feature tracking tools for magnetic flux cancellations and RBEs. For the cancellation tracking, we develop a dedicated algorithm, which uses the intermediate results of SWAMIS as input and can provide more accurate results compared to the standard SWAMIS code on the same magnetograms. For RBEs tracking, our tool is able to detect RBEs in Hα spectral images even if slight image distortion and non-uniform background are present.

Our tools are functioning well when applied to the coordinated observations of *Hinode*/NFI and NSO/IBIS. Magnetic cancellations detected by our tool are concentrated on the magnetic network boundaries as expected. Statistically, our results show similar properties of RBEs compared to previous studies (Wang et al. 1998; Rouppe van der Voort et al. 2009; Sekse et al. 2013a). Furthermore, we investigate the potential relation between magnetic cancellations and RBEs. The results present that magnetic cancellations and RBEs are spatially correlated to the certain extent; however, their temporal correlation is hard to be established, due to very frequent occurrence of RBEs and long lasting magnetic flux cancellation.

CHAPTER 5

THERMODYNAMICS OF SUPRA-ARCADE DOWNFLOWS IN SOLAR FLARES

5.1 Introduction

Solar flares are among the most energetic solar activities, and have been under intensive investigation in increasing details with the improvement in instruments. Despite years of study, some processes and features in flares remain poorly understood, among them are supra-arcade downflows (SADs; McKenzie & Hudson 1999; Innes et al. 2003; Asai et al. 2004). SADs are tadpole-like dark voids falling sunward through the fan-shaped, haze-like flare plasma above the flare arcade (also referred to as "supra-arcade fan" in the literature) in soft X-rays (SXRs) and EUV. They are generally considered as a signature of the outflow of magnetic reconnections occurring high in corona. Their presence is found to be co-temporal with HXR and microwave bursts, which implies their close relation to the impulsive release of magnetic free energy (Asai et al. 2004; Khan et al. 2007).

SADs are not likely to be rare in flares, however, their detection requires specific conditions. As a faint structure, SADs are preferentially seen against a bright background emission (generally the haze region). Besides, they could be obscured by a bright structures in the foreground due to the optically thin nature of SXR or EUV in corona. Therefore, the observation of SADs are almost exclusive to the limb flares (Savage & McKenzie 2011), whose flare arcade is oriented in the North-South direction, so that the axis of the arcade is perpendicular to LOS.

Numerous samples of SADs have been studied for their kinematics in the last decade. At the height where SADs are observed, their velocities are spread from several dozens to a few hundred kilometers per second without significant acceleration or deceleration for each individual SAD (McKenzie & Savage 2009, 2011). As more cases have been studied using various instruments, the interpretations of SAD are also evolving. Early on SAD was assumed to be the cross-section of an evacuated magnetic flux tube (McKenzie 2000; McKenzie & Savage 2009). Recently, Savage et al. (2012) reinterpreted SAD as the wake, i.e., the trailing region of a retracting magnetic flux tube. Although this may explain certain aspects of observations, the physics involved in this reinterpretation remains obscure (Scott et al. 2013). More recently, Liu (2013) suggested SAD as a twisted mini-flux rope which is highly stretched above the cusp region before it finally shrinks and untwists to become a flare loop.

The plasma properties of SADs, which are critical in the exploration of their physical mechanism, become more feasible using models or derived from observations in recent years. Previously SADs were conjectured as evacuated flux tubes, which implies that they would be less dense and hotter than the surrounding plasma (McKenzie & Hudson 1999). In recent years, on one hand, through MHD modeling, Maglione et al. (2011) and Cécere et al. (2012) simulated a similar sunward void structure caused by the interaction of shocks with expansive waves during the reconnection. In their models, these SAD-like voids are of low densities, high beta values and high temperatures that could reach more than 80 MK (Maglione et al. 2011) or 20-30 MK (Cécere et al. 2012). On the other hand, based on the high-cadence multi-wavelengths observations provided by AIA onboard the recently launched SDO, the plasma density and temperature can be recovered using DEM method. The emission measure of observed SADs is lower than the surrounding plasma, as expected for a density depletion (Savage et al. 2012; Hanneman & Reeves 2014). Further, Hanneman & Reeves (2014) found that SADs are generally cooler than the surrounding plasma at around 10 MK. In addition to SDO/AIA, the authors included *Hinode*/XRT which is sensitive to a hotter temperature range (10-100 MK) but there is still no evidence of an extremely hot component exceeding 20 MK present in the DEM of SADs.

The mechanism of SAD has been under active investigation, especially via modeling and simulation in recent years. Scott et al. (2013) supported the interpretation of SAD as a flux tube embedded within the current sheet descending toward the solar surface (Savage et al. 2012). Their simulation shows that a region of depletion follows the shock in front of the descending flux tube. Cassak et al. (2013) suggested that the reconnection is temporally continuous, resulting in sustained void channels that would not be filled by surrounding high density plasma. However, it is noted that the occurrence height of these void channels and the preferred LOS to detect them, which is parallel to the axis of flare arcade, are inconsistent with the observations of SADs (Guo et al. 2014). Further, using SDO/AIA, Innes et al. (2014) found that SADs are not necessarily following an emission enhancement or a retracting loop. More recently, Guo et al. (2014) demonstrated that Rayleigh-Taylor instabilities in the downstream region of the reconnecting current sheet are a promising mechanism of SADs. Their simulated AIA 131 Å data compare favorably with the SADs observed between spike-like bright plasma (Innes et al. 2014). Meanwhile, Cécere et al. (2015)

suggested that a turbulent current sheet resulted from a combination of the tearing mode and Kelvin-Helmholtz instabilities would play an important role to produce SADs.

In this section, we analyze several well-observed SADs from two flare events, using SDO/AIA. A newly developed DEM method (Hannah & Kontar 2012, 2013) is employed to diagnose their thermal properties. In regard to the DEM-weighted temperature, it has been found that the DEM contributed by SAD itself is negligible, which corroborates that SADs are density depletion.

5.2 Data Processing

This study is based on the data obtained by AIA onboard SDO. AIA contains 10 EUV and UV channels covering a full-disk field of view (FOV; up to ∼1.3 $R_\odot$) with a spatial resolution of $\sim 1''$s. The six EUV channels (94 Å , 131 Å, 171 Å, 193 Å, 211 Å, 335 Å), taking images at a high cadence of 12 sec, are sensitive to a variety of coronal temperatures (from $10^{5.5}$ K to $10^{7.5}$ K). We processed the AIA level-1.0 data with the SolarSoftWare (SSW) procedures, `aia_deconvolve_richardsonlucy.pro` and `aia_prep.pro`, to produce level 1.6 data. The Point Spread Function for deconvolution is calculated by `aia_calc_psf.pro`.

We investigated two flares in this study and one of them, the 2013 October 2 event, is coincident with a scheduled calibration of the Helioseismic and Magnetic Imager (HMI) onboard SDO. For the AIA images, this calibration caused bad frames lasting about 2 minutes every 12 minutes due to the rotation of the telescope. The cadence of AIA EUV channels is also extended to 20 seconds during the calibration.

Except those bad frames, the AIA image quality is normal and stable. Thus, for this particular event, we performed an additional process that removed all the bad frames and carefully aligned the limb position for each channel. There is no such a complication in the other event, the 2014 Apr 2 flare. The most recent available AIA temperature response functions are used (V4 calibration), which applying both the CHIANTI fix [1] to account for missing emission lines in the CHIANTI database in channels 94 and 131 Å and EVE normalization to give good agreement with full-disk EVE spectral irradiance data.

As mentioned in Section 3.4, we employ DEM analysis using the enhanced regularization method developed by Hannah & Kontar (2012). In particular, 12 temperature bins, namely, [0.5-1], [1-1.5], [1.5-2], [2-3], [3-4], [4-6], [6-8], [8-11], [11-14], [14-19], [19-25] & [25-32] MK, are selected to carry out the DEM analysis. For selected regions of interest (ROIs), we further calculated the average DEM of each region and the corresponding uncertainty, following the rule of error propagation.

5.3 Results

5.3.1 2013 October 2 Event

The flare occurred on the northwestern limb in NOAA AR 11850 at around 20:00 UT on 2013 October 2. It is a GOES-class C1 flare which is partially occulted by the solar limb. The axis of the flare arcade is oriented almost in the longitudinal direction and located very close to the limb. As a result, the arcade is observed from a side-on

---

[1] http://sohowww.nascom.nasa.gov/solarsoft/sdo/aia/response/chiantifix_notes.txt

perspective, with a large number of dark SADs flowing through the bright fan-shaped haze from 20:50 UT to 00:50 UT on the next day (Oct 3).

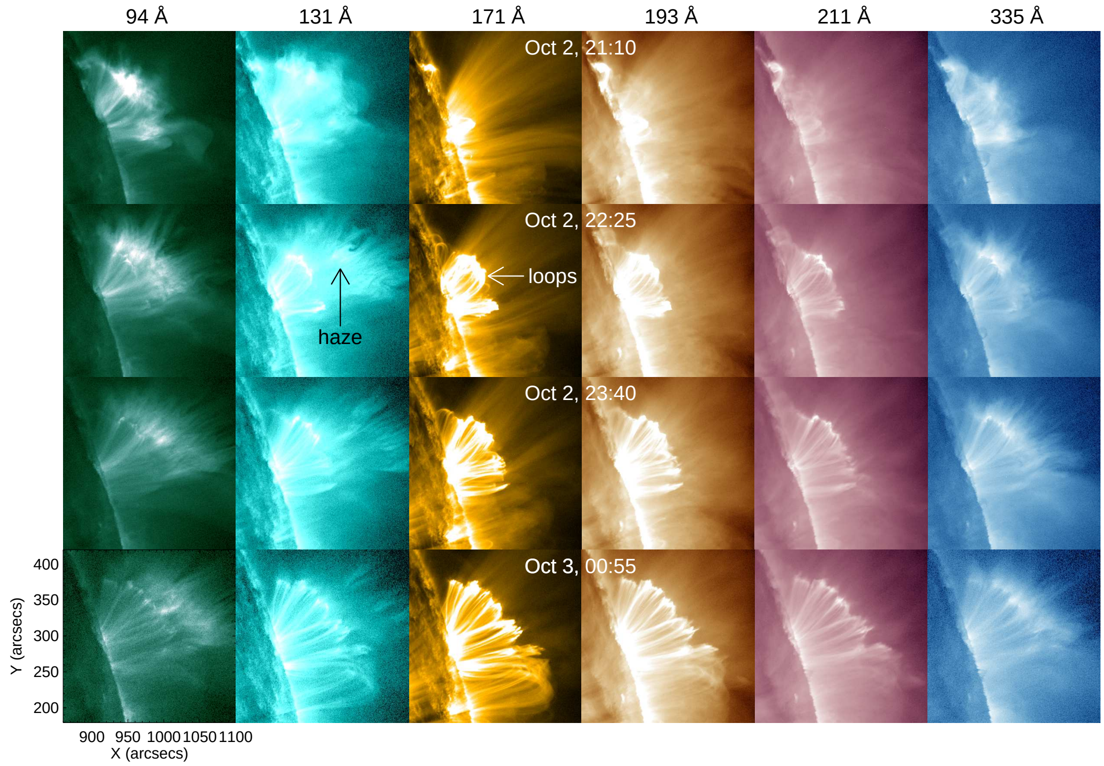

Figure 5.1 Snapshots of AIA images featuring the postflare loops forming sequence. From top to bottom, each row presents multi-wavelengths of AIA images every 75 minutes, which shows that the postflare loops first appeared in the north side and later expanded southward, most obviously in AIA 171 Å.

In this event, SADs generally exhibit a tadpole shape against the background. When an SAD plunges into the bright haze region, the "head" of the tadpole is apparently compressed into a smaller size. Some SADs do not have a clear wiggling "tail" but an elongated ray behind the falling "head". These tailing features last several minutes and gradually shrink before disappearing eventually. SADs are seen first above the northern edge of this AR at around N23° at about 21:00 UT in the AIA 131 Å channel. In the following 2 hours, the locations where they first appear

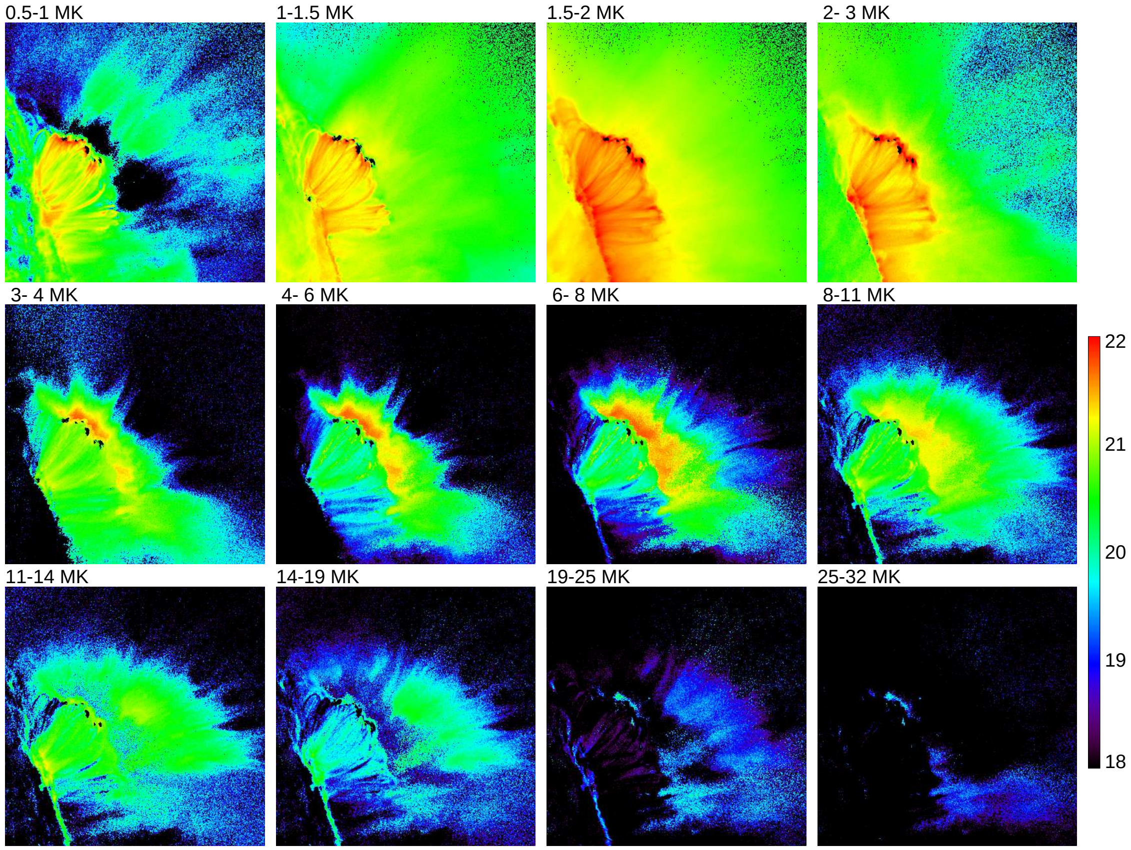

Figure 5.2 DEM maps in different temperature ranges for the 2013 Oct 2 event at 22:45:35 UT. The color scale shows the logarithm of DEM in units of cm^{-5} K^{-1}.

gradually migrate southward (between N15° ∼N18°, see movie311). Earlier SADs are not only smaller in size, but also travel along shorter and more curved orbits, compared to those observed later. Similarly, we found that the post-flare loops (PFLs) form sequentially in a North-South direction, as shown in Figure 5.1. This successive formation of PFLs span a longer time period (∼4 hours) than the migration of SADs. There is only a few PFLs appeared earlier in the low latitude region.

The DEM method is employed to diagnose the density and temperature of SADs (Figure 5.2 and 5.3). At around 21:00 UT, the first SAD of interest (SAD1) is observed in AIA 131 Å (Figure 5.4). We selected a few ROIs for the DEM analysis,

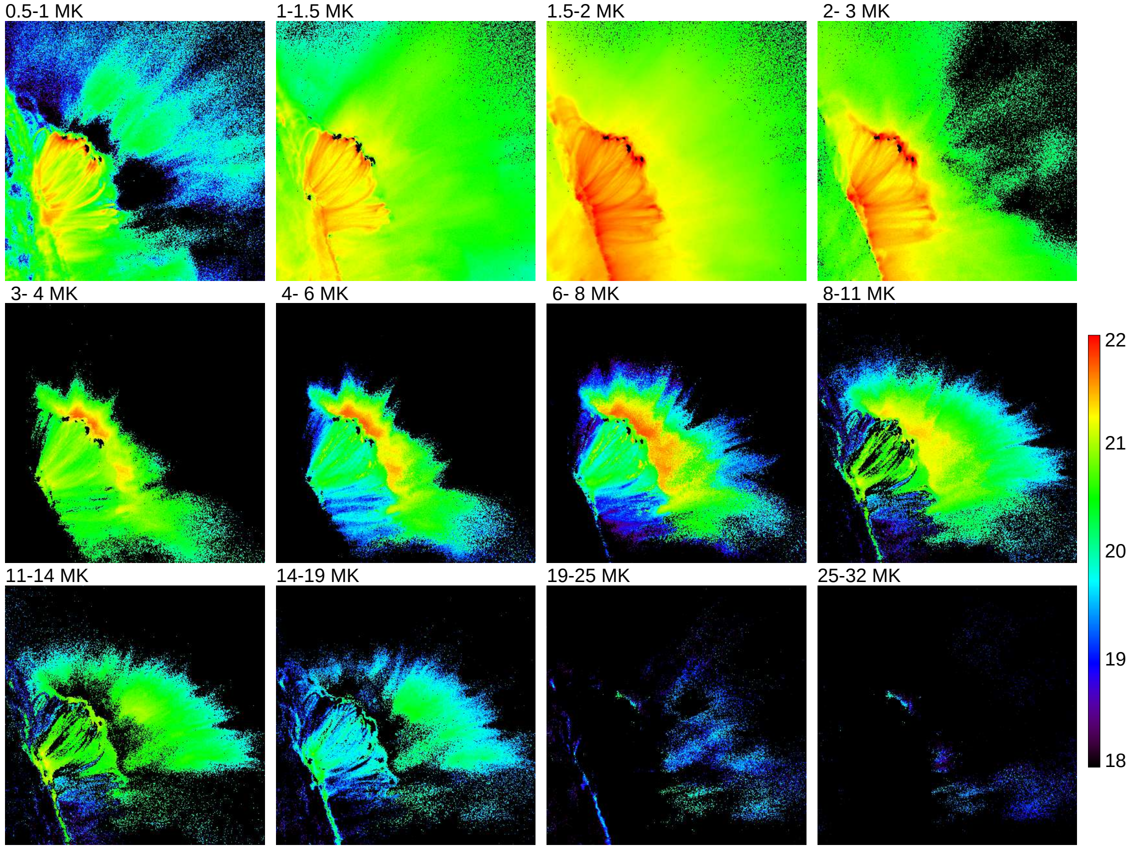

Figure 5.3 Filtered DEM maps in different temperature ranges for the 2013 Oct 2 event at 22:45:35 UT. It removes pixels with relatively large uncertainty ($log(\mathrm{DEM}) >$ 30% or $log(T) > 0.25$) from Figure 5.2. The color scale shows $log(\mathrm{DEM})$ in units of cm^{-5} K^{-1}.

including a region on the path of SAD1 ($\mathrm{R}_{\mathrm{SAD1}}$), a neighboring region in the haze ($\mathrm{R}_{\mathrm{haze1}}$) and a reference region in the quiet corona at the same height as SAD1 ($\mathrm{R}_{\mathrm{ref1}}$). Figure 5.4(b) shows a snapshot when SAD1 is passing through $\mathrm{R}_{\mathrm{SAD1}}$, as well as shortly before (Figure 5.4(a)) and after (Figure 5.4(c)) the passage. The corresponding DEM profiles are plotted in Figure 5.4(d)-(f). The DEM profile below 4 MK is similar for all ROIs and remain temporally unchanged, which is assumed to account for the coronal background along the LOS. In this study, we focus on the hot (>4 MK) DEM component ($\mathrm{DEM}_{\mathrm{h}}$ hereafter) which is associated with flaring plasma

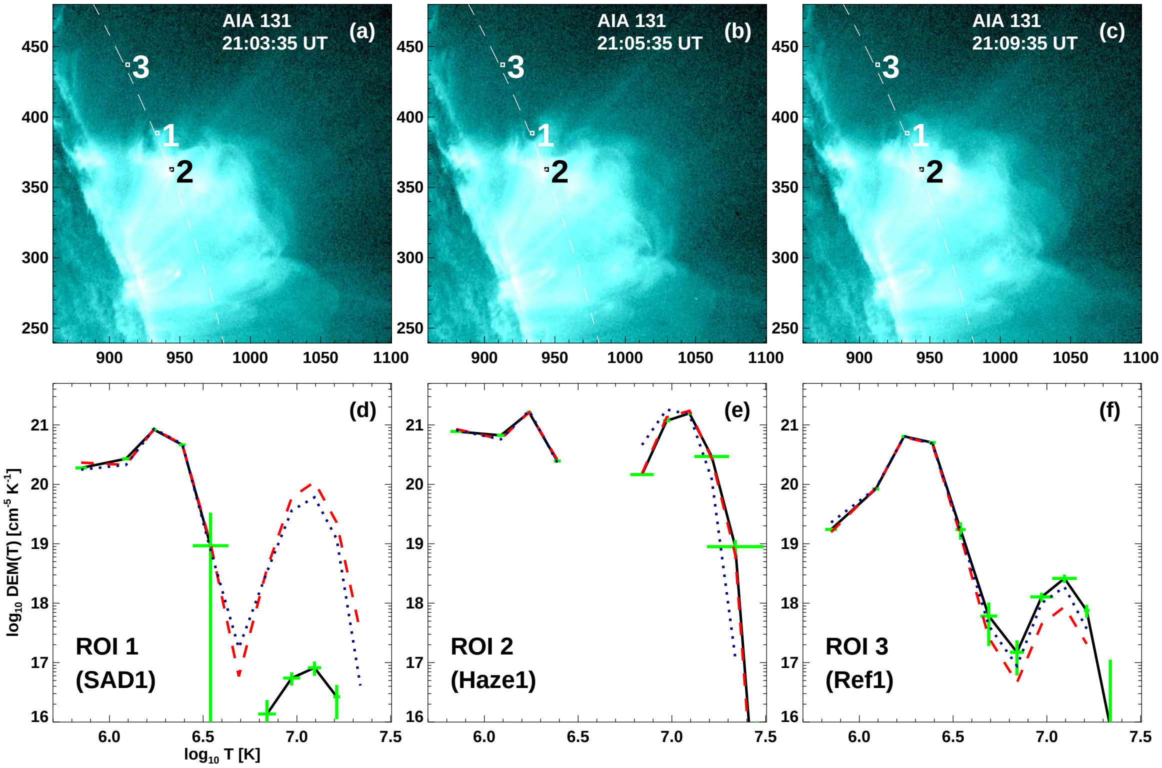

Figure 5.4 DEM analysis for an SAD appearing at around 21:05 UT on 2013 October 2. Panels (a)-(c) show snapshots of AIA 131 Å images before, during and after the SAD passed through ROI1. Panels (d)-(f) show DEM plots for R_{SAD1}, R_{haze1} and R_{ref1}, respectively ($3'' \times 3''$ each); the red dashed lines correspond to 21:03 UT (panel (a)); the black solid lines correspond to 21:05 UT (panel (b)) with green error bars; and the blue dotted lines correspond to 21:09 UT (panel (c)).

and modulated by the passing SADs. For R_{SAD1}, it is clear that there is a significant drop in DEM_h, by about three orders of magnitude, and then DEM_h totally recovers soon after SAD1 passed through. When SAD1 is located within R_{SAD1}, DEM_h is reduced to a value even smaller than that in R_{ref1}, but the peak temperature of DEM_h remains unchanged at around 11-14 MK in spite of the drop in DEM_h. In addition, there is no sign of SAD1 having a high temperature component exceeding 20 MK. DEM_h in R_{SAD1} before and after the passage is one order of magnitude smaller

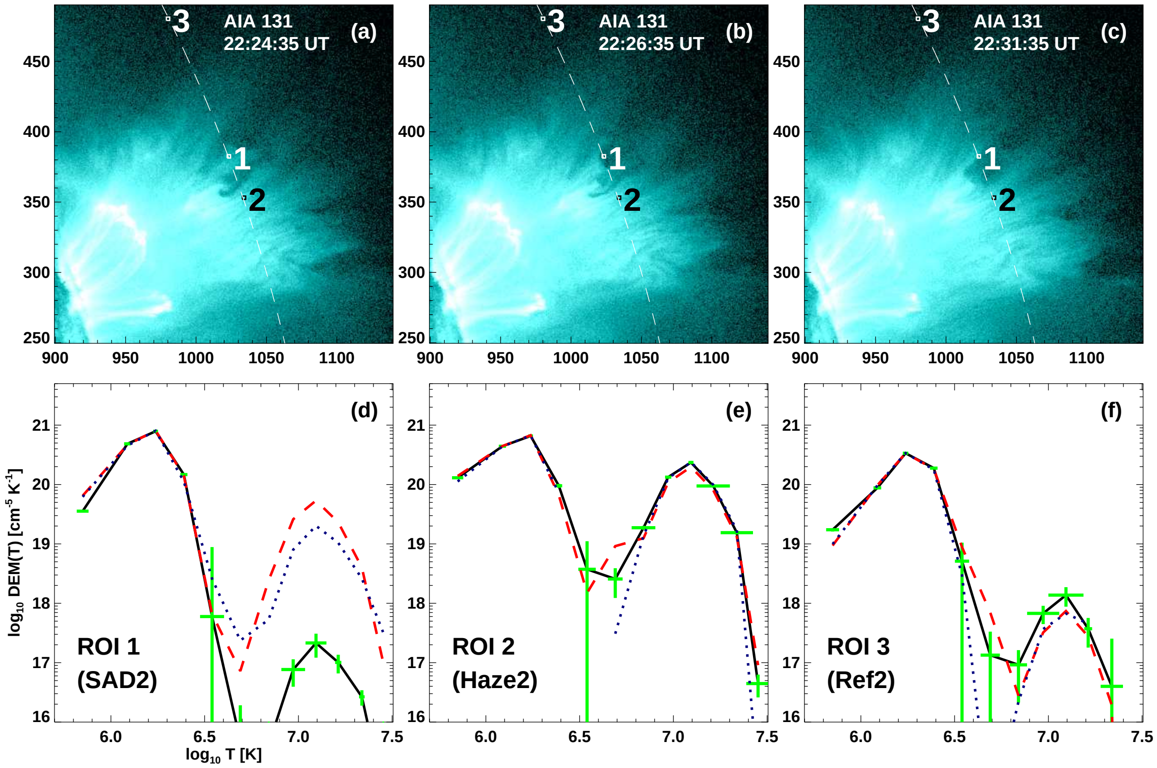

Figure 5.5 DEM analysis for an SAD appearing at around 22:26 UT on 2013 October 2. Panels (a)-(c) show snapshots of AIA 131 Å images before, during and after the SAD passed through ROI1. Panels (d)-(f) show DEM plots for R_{SAD2}, R_{haze2} and R_{ref2}, respectively ($3'' \times 3''$ each); the red dashed lines correspond to 22:24 UT (panel (a)); the black solid lines correspond to 22:26 UT (panel (b)) with green error bars; and the blue dotted lines correspond to 22:31 UT (panel (c)).

than R_{haze1}, the core of the haze region, probably because R_{SAD1} is located at the edge of the haze region.

Through analyzing the DEM of a few more SADs observed later in this event, we found that generally they share similar characteristics. Figure 5.5 shows one SAD (SAD2) at around 22:26 UT and Figure 5.6 shows two SADs (SAD3a and SAD3b) at around 22:45 UT. For ROIs with passing SADs (R_{SAD2}, R_{SAD3a} and R_{SAD3b}), their profiles all present a significant drop when an SAD is passing and then fully recovers within a few minutes after the SAD left the region of interest (ROI). DEM_h in the

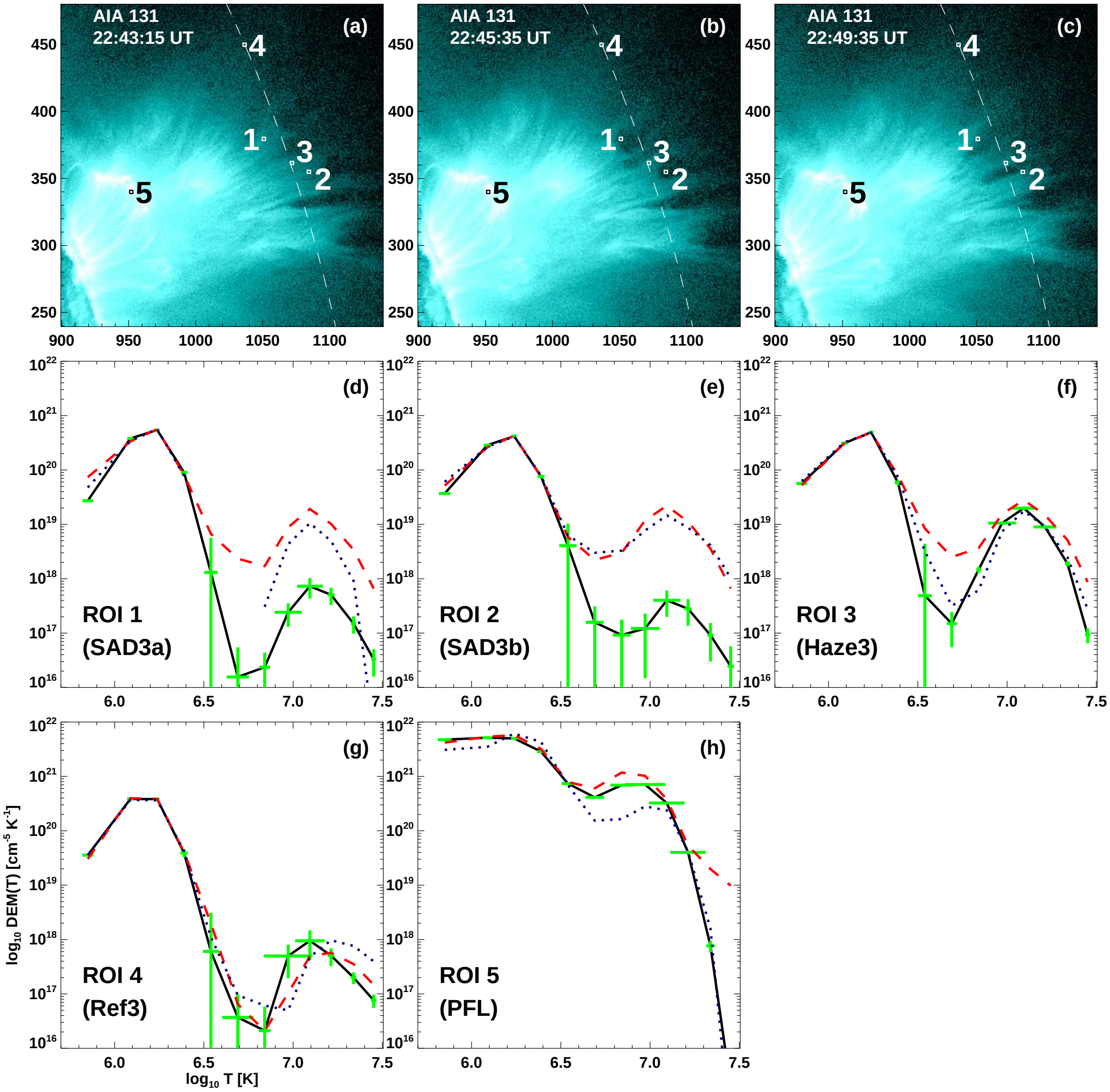

Figure 5.6 DEM analysis for two SADs, 3a and 3b, appearing at around 22:45 UT on 2013 October 2. Panels (a)-(c) show snapshots of AIA 131 Å images before, during and after the SADs passed through ROI1 and ROI2. Panels (d)-(h) show DEM plots for R_{SAD3a}, R_{SAD3b}, R_{haze3}, R_{ref3} and R_{pfl}, respectively ($3'' \times 3''$ each); the red dashed lines correspond to 22:43 UT (panel (a)); the black solid lines correspond to 22:45 UT (panel (b)) with green error bars; and the blue dotted lines correspond to 22:49 UT (panel (c)).

reference region (R_{ref2} and R_{ref3}) is as weak as those in the ROIs with the presence of SADs. The DEM_h of haze regions (R_{haze2} and R_{haze3}) is similar as that in the corresponding $\mathrm{R_{SAD}}$ when the SAD is not inside the region. The $\mathrm{DEM_h}$ still peaks at 11-14 MK for all regions except in the post-flare loops (PFLs) region ($\mathrm{R_{pfl}}$), whose $\mathrm{DEM_h}$ is apparently shifted leftward, indicating a cooler temperature consistent with the standard picture.

5.3.2 2014 April 2 Event

This GOES M6.5 flare occurred at around 14:00 UT at N14E53 in NOAA AR 12027. The flare arcade is formed following a filament eruption and has a curved "L" shape. Accordingly, SDO's LOS for this event is oblique to the axis of the flare arcade. Several comet-tail-like bright spikes semi-parallel to each other are located above the top of the flare arcade. Meantime, SADs are observed to flow between those sheets, most obviously during 14:50 - 16:20 UT.

The SADs in this event still show a tadpole-like shape in AIA 131 Å observations and fade in the bright haze in a few minutes. It is clear in running difference images separated by ∼1 min that the reduction in brightness due to the SAD "head" is generally tailed by an enhancement when the plasma recovers to the normal coronal condition. The sizes of SADs appear to be smaller in comparison to the 2013 Oct 2 event probably because of the oblique viewing angle. The supra-arcade region seems to provide stronger contrast in this event, hence almost every SAD is followed by its "tail". We noted that sometimes the SADs cluster and fall sequentially on a similar path. However, the followers are not necessarily moving along the "tails" of the leaders, because the observed emission is integrated along the LOS (see discussion in Section 5.4).

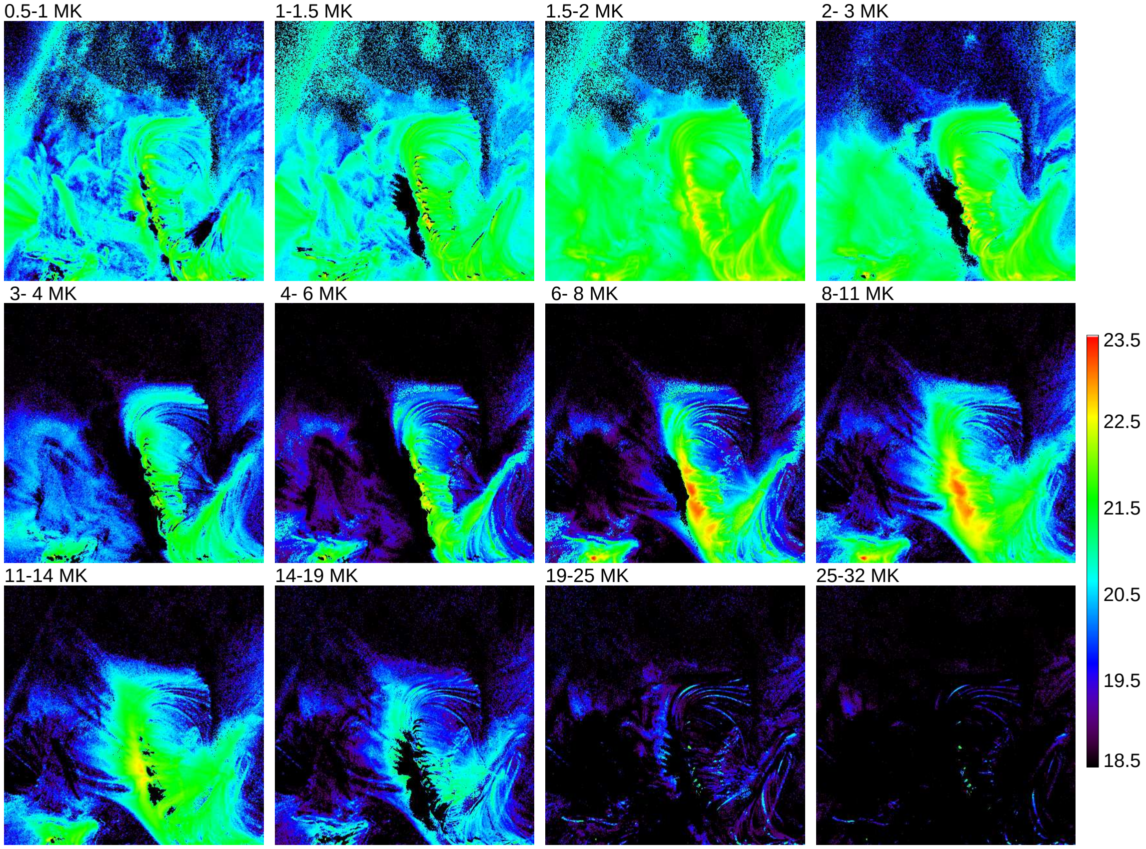

Figure 5.7 DEM maps in different temperature ranges for the 2014 Apr 2 event at 15:13:41 UT. The color scale shows the logarithm of DEM in units of cm^{-5} K^{-1}.

The DEM analysis of SADs in this event does not show any major difference from the 2013 Oct 2 event (Figure 5.7 and 5.8). One case at around 15:02 UT is shown in Figure 5.9 and another case at around 15:13 UT in Figure 5.10. During the passage of SADs, DEM$_\mathrm{h}$ within the ROIs on the path of SADs (R$_\mathrm{SAD4}$ and R$_\mathrm{SAD5}$) are significantly decreased by about one order of magnitude and then recovered soon after that. The magnitude of decrease is smaller than the 2013 Oct 2 event, probably due to the oblique viewing angle in this event, resulting in the presence of more hot and dense haze plasma along the LOS. When SADs are not passing through the aforementioned ROIs, their DEM$_\mathrm{h}$ are very similar to the nearby ROIs (R$_\mathrm{haze4}$ and

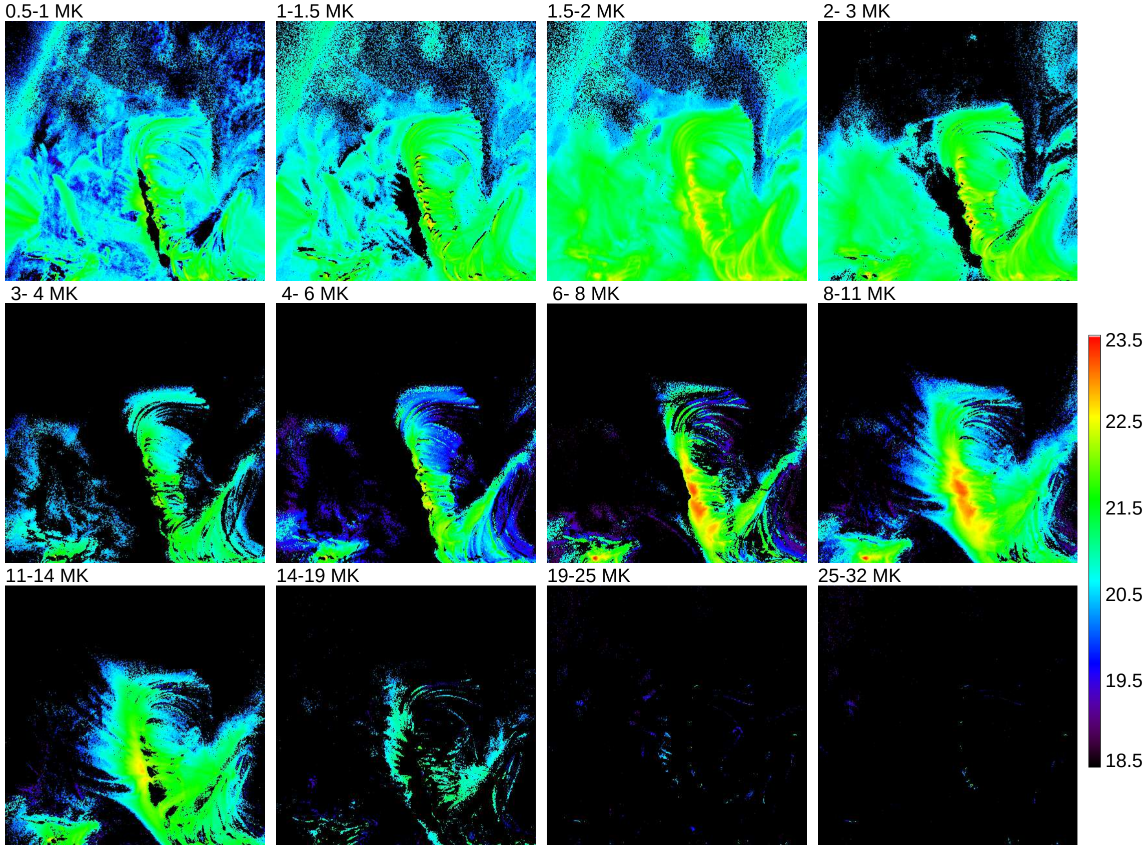

Figure 5.8 Filtered DEM maps in different temperature ranges for the 2014 Apr 2 event at 15:13:41 UT. It removes pixels with relatively large uncertainty ($log(\text{DEM}) > 30\%$ or $log(T) > 0.25$) from Figure 5.7. The color scale shows $log(\text{DEM})$ in units of $\text{cm}^{-5}\ \text{K}^{-1}$.

R_{haze5}) that are located in the bright spikes. In addition, the peak temperature of all DEM_{h} is again more or less stable over time at around 11-14 MK. None of ROIs presents any significant DEM beyond 20 MK.

5.4 Summary and Discussion

Because the corona is optically thin, the obtained DEM contains contribution not only from the volume occupied by the SAD but also from the rest of the column of plasma along the LOS. The DEMs in the flaring region usually have a double-peak profile and

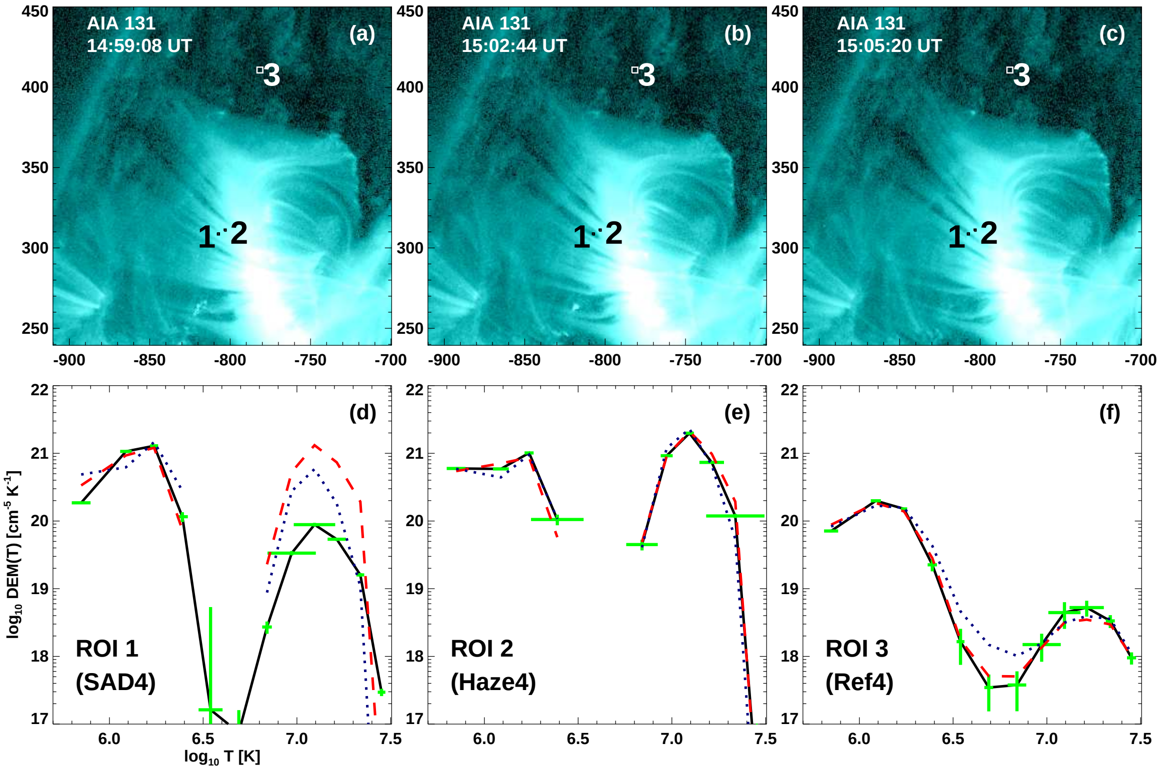

Figure 5.9 DEM analysis for an SAD appearing at around 15:02 UT on 2014 April 2. Panels (a)-(c) show snapshots of AIA 131 Å images before, during and after the SAD passed through ROI1. Panels (d)-(f) show DEM plots for $R_{\rm SAD4}$ ($1\farcs8 \times 1\farcs8$), $R_{\rm haze4}$ ($1\farcs8 \times 1\farcs8$) and $R_{\rm ref4}$ ($4\farcs2 \times 4\farcs2$); the red dashed lines correspond to 14:59 UT (panel (a)); the black solid lines correspond to 15:02 UT (panel (b)) with green error bars; and the blue dotted lines correspond to 15:05 UT (panel (c)).

the low temperature component persistently peaks at 1-2 MK. We conclude that this cooler component is mostly contributed by the foreground and background plasma in the quiet corona along the LOS, in agreement with Hannah & Kontar (2013). Therefore, in this study, the aforementioned $\rm DEM_h$ (DEM component at 4-32 MK) is utilized to analyze SADs.

Each of the six studied SADs from the two flares has a similar pattern on the evolution of the $\rm DEM_h$ profile, i.e., a significant depression of the DEM in the temperature range of 4-32 MK, presumably due to the density depletion. This

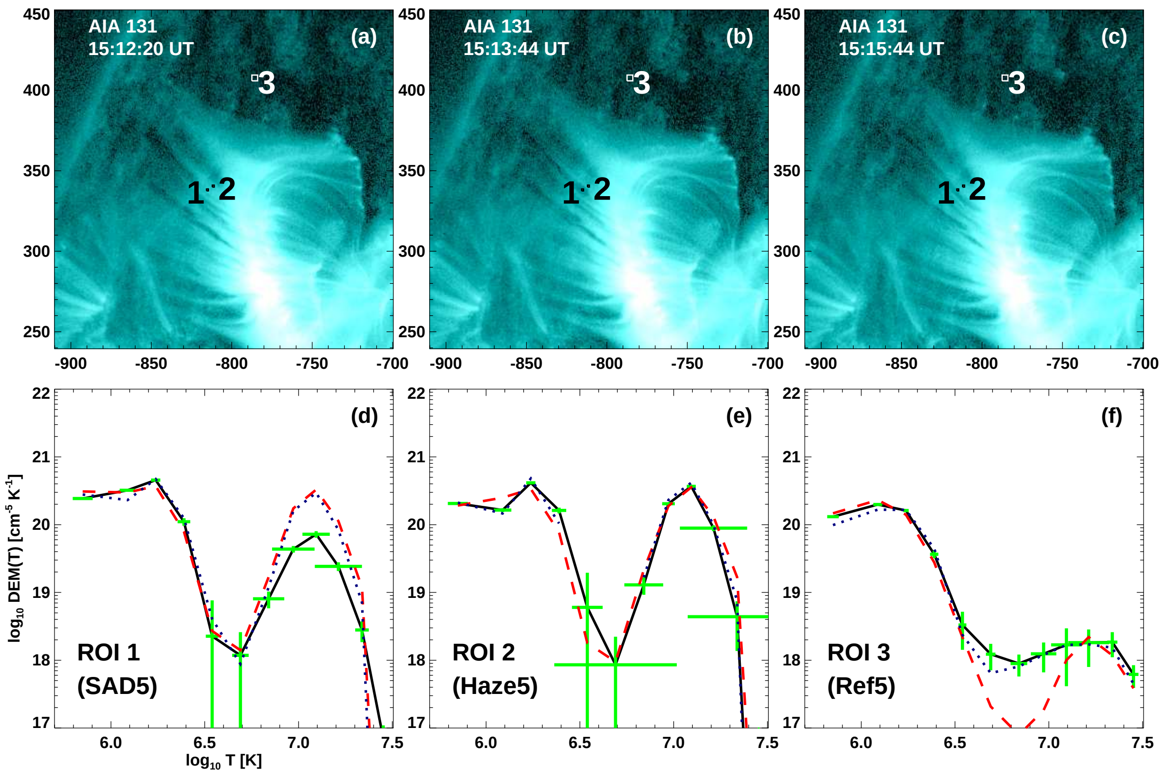

Figure 5.10 DEM analysis for an SAD appearing at around 15:13 UT on 2014 April 2. Panels (a)-(c) show snapshots of AIA 131 Å images before, during and after the SAD passed through ROI1. Panels (d)-(f) show DEM plots for R_{SAD5} ($1''.8 \times 1''.8$), R_{haze5} ($1''.8 \times 1''.8$) and R_{ref5} ($4''.2 \times 4''.2$); the red dashed lines correspond to 15:12 UT (panel (a)); the black solid lines correspond to 15:13 UT (panel (b)) with green error bars; and the blue dotted lines correspond to 15:15 UT (panel (c)).

depression of $\mathrm{DEM_h}$ suggests that at the detected altitude, SADs must have replaced most of the hot haze that would otherwise occupy the LOS volume, i.e., they must have similar LOS depths as the supra-arcade haze, and furthermore they must be much more rarefied than the hot haze. Apparently this depression could be affected by the LOS direction, as demonstrated by the different magnitude of depression between the 2 events studied. In the 2014 Apr 2 event, due to the oblique viewing angle, there is more haze projected in front of or behind the SADs along the LOS, resulting in a weaker depression of $\mathrm{DEM_h}$ than in the 2013 Oct 2 event.

Table 5.1 List of $\langle T\rangle_{\mathrm{h}}$ (in MK) for $\mathrm{R_{SAD}}$s

Passage of SADs	Before	During	After
$\mathrm{R_{SAD1}}$	12.3±1.0	12.3±3.7	12.1±1.4
$\mathrm{R_{SAD2}}$	13.6±1.2	14.3±4.5	14.5±1.4
$\mathrm{R_{SAD3a}}$	14.5±1.5	15.5±4.4	13.3±1.8
$\mathrm{R_{SAD3b}}$	14.2±1.9	14.7±9.0	14.3±2.4
$\mathrm{R_{SAD4}}$	14.5±2.4	14.8±1.5	13.0±1.6
$\mathrm{R_{SAD5}}$	13.0±1.9	12.8±2.0	12.8±1.4

Except for the depressed intensity, SAD presents negligible impact on the temperature distribution of the DEM profile. This has been further quantified using the DEM-weighted mean temperature defined conventionally as follows,

$$\langle T\rangle = \frac{\sum DEM(T) \times T\Delta T}{\sum DEM(T)\Delta T}, \tag{5.1}$$

For $\mathrm{DEM_h}$ in this study, we select 4-32 MK as the sum interval to calculate $\langle T\rangle_{\mathrm{h}}$ (Gou et al. 2015). Table 5.1 lists $\langle T\rangle_{\mathrm{h}}$ within all $\mathrm{R_{SAD}}$s before, during and after the passage of SADs. Generally, for each ROIs, $\langle T\rangle_{\mathrm{h}}$ remains almost unchanged during the investigated period. Although it seems that SAD2 slightly increased $\langle T\rangle_{\mathrm{h}}$ of $\mathrm{R_{SAD2}}$ while SAD3a and SAD4 slightly decreased $\langle T\rangle_{\mathrm{h}}$ of the corresponding ROIs, these changes are within the uncertainties introduced by the DEM. Hanneman & Reeves (2014), using `xrt_dem_iterative2.pro` in SSW, suggested that SADs are cooler than the surrounding plasma but hotter than the coronal background, based on the peak temperature of the DEM profile. One must be aware that most likely, with the LOS integration effect, neither the peak temperature nor $\langle T \rangle_{\mathrm{h}}$ represent the temperature of SAD itself, but the temperature of the remaining haze along the LOS.

In comparison with numerical simulations, we found no indication of enhancement of $\mathrm{DEM_h}$ ahead of the SADs in either flare studied, in agreement with the observations by Innes et al. (2014), which cannot be reconciled with the rarefied wake of a high-emission shock in the simulation by Scott et al. (2013). We found that the SAD-associated depression of $\mathrm{DEM_h}$ can be recovered within a few minutes. In the 2014 April 2 flare, there are occasions that SADs apparently fall sequentially through the same route, but it is possible that different routes are aligned along the LOS which is oblique to the axis of the flare arcade. Therefore, it may not be necessary to resort to continuous reconnections to keep SADs from being filled from behind as in Cassak et al. (2013), if they are inherently discrete features. It has also been noticed that the high-density structures between the emulated SADs in Guo et al. (2014) are finger-like and dynamic while the SADs in the 2014 Apr 2 event flow between spike-like, stable structures.

As far as plasma properties are concerned, the simulated SADs in Guo et al. (2014) and Cécere et al. (2015) have similar characteristics, which are of low density ($1/3 - 1/2$ of the surroundings) but high temperature (more than 20 MK). However, EM of the simulated SADs is only one order of magnitude smaller than the surroundings, and should therefore manifest as a bump in the tail of the DEM profile, resulting in an increase in $\langle T \rangle_{\mathrm{h}}$. In contrast, our results show that $\mathrm{DEM_h}$ is depressed by more than one order of magnitude but $\langle T \rangle_{\mathrm{h}}$ remains more or less constant with the presence of

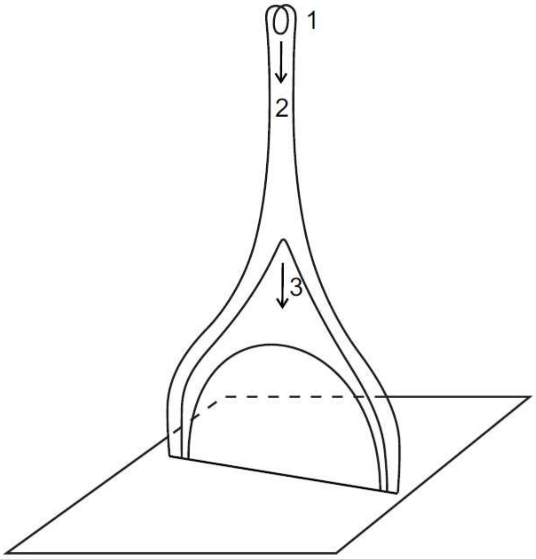

Figure 5.11 Schematic of a twisted mini flux rope showing as an SAD. The numbers indicate three evolving stages of the flux rope. 1) A mini flux rope forms in twisted at the top of reconnected flux tube; 2) the highly stretched flux rope evolves into a cusp-like loop, which exhibits as the appearance and disappearance of an SAD; 3) the cusp-like loop evolves into an arc-shaped post-flare loop (Liu 2013).

SADs. For instance, $\mathrm{EM_h}$ (integrating $\mathrm{DEM_h}$ over the temperature) is reduced from 10^{27} to 10^{25} (cm^{-5}) with the passage of SAD1. However, one must keep in mind that AIA is insensitive to hot plasma with temperature above 20 MK, so it remains an open question whether SADs have extremely hot temperatures. On the other hand, the high temperature is required to prevent the simulated low-density SADs from being filled by surrounding plasma, but may not be necessary if SADs are magnetic entities with an enhanced magnetic pressure (Liu 2013; see Figure 5.11).

Qualitatively or quantitatively, our results have discrepancies with recent models, which is not surprising. Considering that the simulations seldom take into account thermal conduction and radiative losses, and that the assumption underlying the DEM method, local thermal equilibrium, these may not be valid in the reconnection outflow where SADs are supposedly formed. Further efforts are needed from both observational and theoretical aspects to improve the understanding of SADs.

CHAPTER 6

SUMMARY OF THE DISSERTATION AND FUTURE PERSPECTIVES

This dissertation combines studies from two aspects, the small-scale dynamics and the large-scale flare associated phenomena, both of them are related to magnetic reconnection process. On one hand, small-scale dynamics in the solar atmosphere are conceivable to play an important role in the coronal heating problem. To estimate the total attainable energy contribution of small-scale dynamics, it is meaningful to statistically study their characteristics including their occurrence rate. On the other hand, we concentrate on one important aspect of flare-associated magnetic reconnections. The study of SADs using SDO/AIA observations is promising to better understand the key questions during the flaring magnetic reconnections, such as the formation of current sheet. For both aspects of this dissertation, the major results are summarized in the following.

For small-scale dynamics, to study magnetic flux cancellations and RBEs, first the author develops a set of dedicated feature detecting tools and track their properties for each of them. Our specific flux cancellation tracking tool has the capability to detect significantly more events and collect their properties with better precision than its predecessor, SWAMIS. We further develop an RBE tracking tool that can be used on Hα spectral data set, e.g., observations of IBIS. It has enhanced tolerance of image distortion and non-uniform background as designed. Our tools are employed on the coordinated observations using Hinode/NFI and NSO/IBIS. As a result, it is demonstrated that both of them perform well.

Next, we study the statistical properties of the detected RBEs and flux cancellations. For flux cancellations, the results contain the occurrence rate, lifetime, location, and flux variation of cancellation events. Overall cancellation sites exhibit a network pattern that coincides with magnetic network boundaries as expected. For RBEs, their correspondingly properties are found to be similar to previous studies (Wang et al. 1998; Rouppe van der Voort et al. 2009; Sekse et al. 2013a) using different instruments. Finally, we further search for the potential relation between RBEs and cancellations. There are several clear cases of RBEs with associated magnetic flux evolution, however, statistically the correlation is not much better than random coincidence.

For the study of SADs as associated phenomena of flares, the author corroborates that SADs are indeed void of plasma, with negligible DEM. By monitoring the change of DEM with the passage of SADs, we demonstrate, for the first time, that SADs are able to squeeze out the hot and dense haze, so that the hot component of DEM ($>$ 4 MK) is reduced roughly to the coronal background level, without significant change of the profile. We further discussed the discrepancies between our result with several recent models (e.g., Scott et al. 2013; Cassak et al. 2013; Guo et al. 2014; Cécere et al. 2015).

As a concluding remark of this dissertation, there is an outline of the prospective further studies as follows:

- The studies of small-scale dynamics such as RBEs will take great advantages from the new state-of-the-art instruments, especially the 1.6 M New Solar Telescope (NST; Cao et al. 2010) at BBSO. NST is currently the largest solar telescope that achieves an extremely high resolution of $\sim 0.06''$ (in visible) with the aid of its powerful high-order adaptive optic system. Also, the seeing condition of BBSO is one the best of the world which provides consistently-stable observations with a relatively long period. The Visible Imaging Spectrometer (VIS) of NST can observe the chromosphere with similar but more capabilities of IBIS, especially the fast camera of VIS enables the speckle reconstruction to further refine the images. All aspects above indicate the unprecedented view of small-scale dynamics will be revealed by NST. Besides VIS, the Cryogenic Infra-Red Spectrograph (Cyra) of NST will provide high resolution ($\sim 0.2''$) and high cadence (< 1 min) magnetograms in the near future, which enables further studies of photospheric magnetic evolution. In addition, The IRIS (De Pontieu et al. 2014) is a newly launched (June 2013) space telescope which is sensitive to different layers (in temperatures) in the chromosphere and transition region through its UV spectrograph. IRIS also has excellent resolution ($0.33'' \sim 0.4''$) and cadence ($10 \sim 20$ s). It is particularly important to study the evolution of small-scale dynamics as well as their relations with each other. By using data with significantly improved quality with these new instruments, the further studies of small-scale dynamics are promising to show more details and correspondingly discover the inherent mechanism.

- Moreover, as our study mostly concentrates to the quiet sun, further investigations including coronal holes and plages will present more comprehensive results. The experience and algorithm of the feature tracking method in this study can be transplanted for the new instruments. Besides our dedicated tracking tools, the rapid developing computational and imaging processing tools will provide continued advances in science discoveries.
- Meanwhile, for the study of flare associated phenomena, although we present a significant result, it is still waiting for examination with more evidence. Thus, a statistical study of thermodynamic properties containing more SADs is needed. Furthermore, for modeling related to current sheet and SAD, a combined modeling and observational effort is needed. For example, using SDO/AIA observations, Liu (2013) conjectures that SADs as magnetic entities after reconnections, which are highly stretched mini-flux ropes with enhanced magnetic pressure. A numerical simulation based on this interpretation would be important to provide an integrated view of SADs.

REFERENCES

Antiochos, S. K., DeVore, C. R., & Klimchuk, J. A. 1999, The Astrophysical Journal, 510, 485.

Asai, A., Yokoyama, T., Shimojo, M., & Shibata, K. 2004, The Astrophysical Journal Letters, 605, L77.

Aschwanden, M. J. 2006, Physics of the solar corona: an introduction with problems and solutions (Springer in association with Praxis Publishing Ltd, Chichester, UK).

Aschwanden, M. J., & Boerner, P. 2011, The Astrophysical Journal, 732, 81.

Beckers, J. M. 1968, Solar Physics, 3, 367.

Brueckner, G. E., & Bartoe, J.-D. F. 1983, The Astrophysical Journal, 272, 329.

Cao, W., Gorceix, N., Coulter, R., Ahn, K., Rimmele, T. R., & Goode, P. R. 2010, Astronomische Nachrichten, 331, 636.

Carmichael, H. 1964, NASA Special Publication, 50, 451.

Cassak, P. A., Drake, J. F., Gosling, J. T., Phan, T.-D., Shay, M. A., & Shepherd, L. S. 2013, The Astrophysical Journal, 775, L14.

Cavallini, F. 2006, Solar Physics, 236, 415.

Cécere, M., Schneiter, M., Costa, A., Elaskar, S., & Maglione, S. 2012, The Astrophysical Journal, 759, 79.

Cécere, M., Zurbriggen, E., Costa, A., & Schneiter, M. 2015, The Astrophysical Journal, 807, 6.

Chae, J. 1999, in Astronomical Society of the Pacific Conference Series, Vol. 183, High Resolution Solar Physics: Theory, Observations, and Techniques, ed. T. R. Rimmele, K. S. Balasubramaniam, & R. R. Radick, 375.

Chae, J., Moon, Y.-J., Wang, H., & Yun, H. S. 2002, Solar Physics, 207, 73.

Chae, J., Wang, H., Lee, C.-Y., Goode, P. R., & Schuhle, U. 1998, The Astrophysical Journal Letters, 504, L123.

Chen, B., Bastian, T. S., & Gary, D. E. 2014, The Astrophysical Journal, 794, 149.

De Pontieu, B., Carlsson, M., Rouppe van der Voort, L. H. M., Rutten, R. J., Hansteen, V. H., & Watanabe, H. 2012, The Astrophysical Journal Letters, 752, L12.

De Pontieu, B., McIntosh, S. W., Hansteen, V. H., Carlsson, M., Schrijver, C. J., Tarbell, T. D., Title, A. M., Shine, R. A., Suematsu, Y., Tsuneta, S., Katsukawa, Y., Ichimoto, K., Shimizu, T., & Nagata, S. 2007, Publications of Astronomical Society of Japan, 59, 655.

De Pontieu, B., McIntosh, S. W., Carlsson, M., Hansteen, V. H., Tarbell, T. D., Boerner, P., Martinez-Sykora, J., Schrijver, C. J., & Title, A. M. 2011, Science, 331, 55.

De Pontieu, B., Title, A. M., Lemen, J. R., Kushner, G. D., Akin, D. J., Allard, B., Berger, T., Boerner, P., Cheung, M., Chou, C., Drake, J. F., Duncan, D. W., Freeland, S., Heyman, G. F., Hoffman, C., Hurlburt, N. E., Lindgren, R. W., Mathur, D., Rehse, R., Sabolish, D., Seguin, R., Schrijver, C. J., Tarbell, T. D., Wülser, J.-P., Wolfson, C. J., Yanari, C., Mudge, J., Nguyen-Phuc, N., Timmons, R., Bezooijen, R., Weingrod, I., Brookner, R., Butcher, G., Dougherty, B., Eder, J., Knagenhjelm, V., Larsen, S., Mansir, D., Phan, L., Boyle, P., Cheimets, P. N., DeLuca, E. E., Golub, L., Gates, R., Hertz, E., McKillop, S., Park, S., Perry, T., Podgorski, W. A., Reeves, K., Saar, S., Testa, P., Tian, H., Weber, M., Dunn, C., Eccles, S., Jaeggli, S. A., Kankelborg, C. C., Mashburn, K., Pust, N., Springer, L., Carvalho, R., Kleint, L., Marmie, J., Mazmanian, E., Pereira, T. M. D., Sawyer, S., Strong, J., Worden, S. P., Carlsson, M., Hansteen, V. H., Leenaarts, J., Wiesmann, M., Aloise, J., Chu, K.-C., Bush, R. I., Scherrer, P. H., Brekke, P., Martinez-Sykora, J., Lites, B. W., McIntosh, S. W., Uitenbroek, H., Okamoto, T. J., Gummin, M. A., Auker, G., Jerram, P., Pool, P., & Waltham, N. 2014, Solar Physics, 289, 2733.

DeForest, C. E., Hagenaar, H. J., Lamb, D. A., Parnell, C. E., & Welsch, B. T. 2007, The Astrophysical Journal, 666, 576.

Dere, K. P., Bartoe, J. D. F., & Brueckner, G. E. 1989, Solar Physics, 123, 41.

Ellerman, F. 1917, The Astrophysical Journal, 46, 298.

Emilio, M., Kuhn, J. R., Bush, R. I., & Scholl, I. F. 2012, The Astrophysical Journal, 750, 135.

Evershed, J. 1909, Monthly Notices of the Royal Astronomical Society, 69, 454.

Fang, C., Ding, M., & Chen, P. 2008, Physics of Solar Active Regions (Nanjing, PR China: Nanjing University Press).

Forbes, T. G., & Acton, L. W. 1996, The Astrophysical Journal, 459, 330.

Forbes, T. G., & Lin, J. 2000, Journal of Atmospheric and Solar-Terrestrial Physics, 62, 1499.

Forbes, T. G., & Priest, E. R. 1995, The Astrophysical Journal, 446, 377.

Gou, T., Liu, R., & Wang, Y. 2015, Solar Physics, 290, 2211.

Guo, L.-J., Huang, Y.-M., Bhattacharjee, A., & Innes, D. E. 2014, The Astrophysical Journal, 796, L29.

Hannah, I. G., & Kontar, E. P. 2012, Astronomy & Astrophysics, 539, A146.

—. 2013, Astronomy & Astrophysics, 553, A10.

Hanneman, W. J., & Reeves, K. K. 2014, The Astrophysical Journal, 786, 95.

Harvey, J. 1977, Highlights of Astronomy: Part II As Presented at the XVIth General Assembly 1976, ed. E. A. Müller (Dordrecht: Springer Netherlands), 223–239.

Hirayama, T. 1974, Solar Physics, 34, 323.

Hollweg, J., & Buti, B. 1985, Advances in Space Plasma Physics.

Illing, R. M. E., & Hundhausen, A. J. 1985, Journal of Geophysical Research: Space Physics, 90, 275.

Innes, D. E., Guo, L.-J., Bhattacharjee, A., Huang, Y.-M., & Schmit, D. 2014, The Astrophysical Journal, 796, 27.

Innes, D. E., McKenzie, D. E., & Wang, T. 2003, Solar Physics, 217, 247.

Khan, J. I., Bain, H. M., & Fletcher, L. 2007, Astronomy & Astrophysics, 475, 333.

Klimchuk, J. A. 2006, Solar Physics, 234, 41.

Kopp, R. A., & Pneuman, G. W. 1976, Solar Physics, 50, 85.

Lamb, D. A., DeForest, C. E., Hagenaar, H. J., Parnell, C. E., & Welsch, B. T. 2008, The Astrophysical Journal, 674, 520.

—. 2010, The Astrophysical Journal, 720, 1405.

Lamb, D. A., Howard, T. A., DeForest, C. E., Parnell, C. E., & Welsch, B. T. 2013, The Astrophysical Journal, 774, 127.

Langangen, Ø., De Pontieu, B., Carlsson, M., Hansteen, V. H., Cauzzi, G., & Reardon, K. 2008, The Astrophysical Journal Letters, 679, L167.

Lee, C.-Y., Chae, J., & Wang, H. 2000, The Astrophysical Journal, 545, 1124.

Leighton, R. B., Noyes, R. W., & Simon, G. W. 1962, The Astrophysical Journal, 135, 474.

Lemen, J., Title, A., Akin, D., Boerner, P., Chou, C., Drake, J., Duncan, D., Edwards, C., Friedlaender, F., Heyman, G., Hurlburt, N., Katz, N., Kushner, G., Levay, M., Lindgren, R., Mathur, D., McFeaters, E., Mitchell, S., Rehse, R., Schrijver, C., Springer, L., Stern, R., Tarbell, T., Wuelser, J.-P., Wolfson, C., Yanari, C., Bookbinder, J., Cheimets, P., Caldwell, D., Deluca, E., Gates, R., Golub, L., Park, S., Podgorski, W., Bush, R., Scherrer, P., Gummin, M., Smith, P., Auker, G., Jerram, P., Pool, P., Soufli, R., Windt, D., Beardsley, S., Clapp, M., Lang, J., & Waltham, N. 2012, Solar Physics, 275, 17.

Lin, J., & Forbes, T. G. 2000, Journal of Geophysical Research: Space Physics, 105, 2375.

Lin, J., Ko, Y.-K., Sui, L., Raymond, J. C., Stenborg, G. A., Jiang, Y., Zhao, S., & Mancuso, S. 2005, The Astrophysical Journal, 622, 1251.

Lipartito, I., Judge, P. G., Reardon, K., & Cauzzi, G. 2014, The Astrophysical Journal, 785, 109.

Liu, R. 2013, Monthly Notices of the Royal Astronomical Society, 434, 1309.

Livingston, W. C., & Harvey, J. 1975, in BAAS, Vol. 7, Bulletin of the American Astronomical Society, 346.

Maglione, L. S., Schneiter, E. M., Costa, A., & Elaskar, S. 2011, Astronomy & Astrophysics, 527, L5.

Martínez-Sykora, J., Hansteen, V., & Moreno-Insertis, F. 2011, The Astrophysical Journal, 736, 9.

McKenzie, D. E. 2000, Solar Physics, 195, 381.

McKenzie, D. E., & Hudson, H. S. 1999, The Astrophysical Journal Letters, 519, L93.

McKenzie, D. E., & Savage, S. L. 2009, The Astrophysical Journal, 697, 1569.

—. 2011, The Astrophysical Journal, 735, L6.

Moore, R. L., Sterling, A. C., Hudson, H. S., & Lemen, J. R. 2001, The Astrophysical Journal, 552, 833.

Park, S., Chae, J., & Litvinenko, Y. E. 2009, The Astrophysical Journal Letters, 704, L71.

Parker, E. N. 1988, The Astrophysical Journal, 330, 474.

Penn, M. J., & Livingston, W. 2006, The Astrophysical Journal Letters, 649, L45.

Pesnell, W., Thompson, B., & Chamberlin, P. 2012, Solar Physics, 275, 3.

Reardon, K. P., & Cavallini, F. 2008, Astronomy and Astrophysics, 481, 897.

Rouppe van der Voort, L., Leenaarts, J., De Pontieu, B., Carlsson, M., & Vissers, G. 2009, The Astrophysical Journal, 705, 272.

Savage, S. L., & McKenzie, D. E. 2011, The Astrophysical Journal, 730, 98.

Savage, S. L., McKenzie, D. E., & Reeves, K. K. 2012, The Astrophysical Journal, 747, L40.

Schindler, K., & Hornig, G. 2000, Magnetic Reconnection, ed. P. Murdin.

Scott, R. B., Longcope, D. W., & McKenzie, D. E. 2013, The Astrophysical Journal, 776, 54.

Sekse, D. H., Rouppe van der Voort, L., & De Pontieu, B. 2012, The Astrophysical Journal, 752, 108.

—. 2013a, The Astrophysical Journal, 764, 164.

Sekse, D. H., Rouppe van der Voort, L., De Pontieu, B., & Scullion, E. 2013b, The Astrophysical Journal, 769, 44.

Sterling, A. C. 2000, Solar Physics, 196, 79.

Sturrock, P. A. 1966, Nature, 211, 697.

Suematsu, Y., Wang, H., & Zirin, H. 1995, The Astrophysical Journal, 450, 411.

Tsuneta, S., Ichimoto, K., Katsukawa, Y., Nagata, S., Otsubo, M., Shimizu, T., Suematsu, Y., Nakagiri, M., Noguchi, M., Tarbell, T., Title, A., Shine, R., Rosenberg, W., Hoffmann, C., Jurcevich, B., Kushner, G., Levay, M., Lites, B., Elmore, D., Matsushita, T., Kawaguchi, N., Saito, H., Mikami, I., Hill, L. D., & Owens, J. K. 2008, Solar Physics, 249, 167.

van Speybroeck, L. P., Krieger, A. S., & Vaiana, G. S. 1970, Nature, 227, 818.

Vernazza, J. E., Avrett, E. H., & Loeser, R. 1981, Astrophysical Journal Supplement Series, 45, 635.

Wang, H., Johannesson, A., Stage, M., Lee, C., & Zirin, H. 1998, Solar Physics, 178, 55.

Weber, M., Deluca, E., Golub, L., & Sette, A. 2004, in Proceedings of the International Astronomical Union, Vol. 2004, , 321–328.

Yurchyshyn, V., Abramenko, V., & Goode, P. 2013, The Astrophysical Journal, 767, 17.

Zirker, J. B. 1998, Solar Physics, 182, 1.

Zwaan, C. 1987, Annual Review of Astronomy and Astrophysics, 25, 83.